
SPACE-VARIANT TOTAL VARIATION BOOSTED BY LEARNING TECHNIQUES IN FEW-VIEW TOMOGRAPHIC IMAGING

A PREPRINT

Elena Morotti

Department of Political and Social Sciences,
University of Bologna, Italy.
elena.morotti4@unibo.it.

Davide Evangelista

Department of Computer Science and Engineering,
University of Bologna, Italy.

Andrea Sebastiani

Department of Physics, Informatics and Mathematics,
University of Modena and Reggio Emilia, Italy

Elena Loli Piccolomini

Department of Computer Science and Engineering,
University of Bologna, Italy.

ABSTRACT

This paper focuses on the development of a space-variant regularization model for solving an under-determined linear inverse problem. The case study is a medical image reconstruction from few-view tomographic noisy data. The primary objective of the proposed optimization model is to achieve a good balance between denoising and the preservation of fine details and edges, overcoming the performance of the popular and largely used Total Variation (TV) regularization through the application of appropriate pixel-dependent weights. The proposed strategy leverages the role of gradient approximations for the computation of the space-variant TV weights. For this reason, a convolutional neural network is designed, to approximate both the ground truth image and its gradient using an elastic loss function in its training.

Additionally, the paper provides a theoretical analysis of the proposed model, showing the uniqueness of its solution, and illustrates a Chambolle-Pock algorithm tailored to address the specific problem at hand. This comprehensive framework integrates innovative regularization techniques with advanced neural network capabilities, demonstrating promising results in achieving high-quality reconstructions from low-sampled tomographic data.

Keywords Spatially Adaptive Regularization, Space Variant Total Variation, Optimization, Neural Network

1 Introduction

In this work, we consider linear inverse problems of the form:

$$\mathbf{y}^\delta = \mathbf{K}\mathbf{x}^{GT} + \mathbf{e}, \quad \|\mathbf{e}\|_2 \leq \delta, \quad (1)$$

where $\mathbf{x}^{GT} \in \mathcal{X} \subseteq \mathbb{R}^n$ is the (unknown) ground truth image, $\mathbf{K} \in \mathbb{R}^{m \times n}$ is an under-sampled linear operator, i.e. $m \leq n$, $\mathbf{y}^\delta \in \mathbb{R}^m$ is the acquired, noisy datum, and $\mathbf{e} \in \mathbb{R}^m$ is the noise, whose norm is bounded by δ . Note that, since $m \leq n$, the kernel of \mathbf{K} is generally non-trivial, which implies that (1) admits infinite solutions. Moreover, if \mathbf{K} comes from the discretization of an ill-posed integral operator (as it typically happens in imaging), the solutions of (1) do not continuously depend on the data \mathbf{y}^δ . To handle the scarcity of data and the ill-posedness of the problem, a good solution of (1) can be computed by minimizing a regularized problem of the form:

$$\mathbf{x}^* = \arg \min_{\mathbf{x} \in \mathcal{X}} \mathcal{J}(\mathbf{x}, \mathbf{y}^\delta) := \mathcal{F}(\mathbf{x}, \mathbf{y}^\delta) + \lambda \mathcal{R}(\mathbf{x}), \quad (2)$$

where $\mathcal{F}(\mathbf{x}, \mathbf{y}^\delta)$ is the data-fidelity term is utilized to ensure that \mathbf{x}^* aligns with the acquisition model (1) and $\mathcal{R}(\mathbf{x})$ is the regularization term, enforcing stability and uniqueness of the solution by considering prior knowledge on \mathbf{x}^* . The

scalar $\lambda > 0$ controls the contribution of the regularization term over the fidelity one in the overall objective function $\mathcal{J}(\mathbf{x}, \mathbf{y}^\delta)$.

In traditional regularization approaches, $\mathcal{R}(\mathbf{x})$ is applied uniformly to the whole image, i.e. its formulation equally weights the contributions across the pixels. We refer to this case as *global regularization*. Global regularization is simple to implement and computationally low demanding; on the other hand, it treats the entire image as a homogeneous entity making the setting the optimal weight λ not trivial conceptually, because a value may not adapt well to varying characteristics within the image. For instance, a considerably high value of λ may effectively denoise the resulting image within flat regions, yet it could excessively smooth it, potentially leading to the loss or blurring of crucial details in certain areas. Conversely, a slightly lower value might adequately preserve details but fail to sufficiently eliminate noise in uniform areas.

To increase the flexibility of the regularization and better balance the trade-off between denoising and preserving fine details, a good strategy is the *space-variant regularization*. It allows for adapting regularization strength based on local image characteristics. This can enhance the preservation of fine details and edges without losing denoising efficacy, but its implementation is often more complex and computationally intensive than for global methods. In addition, its performance might be more sensitive to noise and artifacts, particularly if the local characteristics are not accurately estimated. In particular, the selection of optimal local regularization parameters is very challenging.

In this work, we explore an imaging application focused on reconstructing medical images from few tomographic measurements. In this case, \mathbf{K} comes from the discretization of the 2-dimensional fan-beam Radon transform and fits the aforementioned properties of ill-posedness. The data perturbations can be modeled with a white additive Gaussian noise, as in (2), hence it is common to set $\mathcal{F}(\mathbf{x}, \mathbf{y}^\delta) = \frac{1}{2} \|\mathbf{K}\mathbf{x} - \mathbf{y}^\delta\|_2^2$ as the data-fitting term. Our task-oriented regularizing prior should preserve diagnostically significant features as well as remove noise. As medical images often contain relevant information in the form of low-contrast objects and boundaries between different anatomical tissues, a common choice for \mathcal{R} is the Total Variation (TV) function. In fact, TV is known to be effective in preserving edges because it penalizes the variation or changes in pixel intensity by promoting sparsity in the gradient image domain [28, 25, 16]. When globally applied, the drawback of TV regularization is the potential introduction of piecewise constant artifacts, which could impact the interpretation of medical information. It is particularly noticeable in regions with smooth intensity variations, as TV regularization tends to oversimplify these areas, resulting in blocky or stair-step artifacts. Furthermore, considering the very restricted number of projections acquired in few-view X-ray examinations (in contrast to conventional imaging protocols), the blocky counteraction can severely promote streaking artifacts caused by the lack of views in the acquisition process.

Contributions. The contributions of this paper are twofold, both theoretical and algorithmic.

Firstly, we demonstrate the uniqueness of the TV-based regularized solution, in the special case where \mathbf{K} is under-determined. It is widely acknowledged that the solution is unique when \mathbf{K} is over-determined; however, to the best of our knowledge, there is no proof in the under-determined case.

Secondly, we introduce a novel model for space-variant Total Variation (TV) regularization. In this model, the TV function’s weights are determined by evaluating the gradient magnitudes of a pre-computed image. We demonstrate that this image should closely approximate the ground truth, particularly within its gradient domain, to get an accurate final solution.

On the algorithmic front, we present several methods for generating the pre-calculated image as a coarse reconstruction from the given observations. When provided with only a single datum \mathbf{y}^δ , we can employ either an analytical or a variational approach for a tomographic problem. Conversely, in cases where the medical scenario provides a dataset comprising consistent pairs of data and accurate reconstructions, we can harness the power of neural networks to generate images with desired features. We have developed a convolutional neural network trained to approximate both the ground truth image and its gradient, utilizing an elastic loss function.

Finally, we tailor the widely recognized Chambolle-Pock algorithm to address the resulting minimization problem. Extensive numerical simulations conducted on both a synthetic image and a real dataset assess the relevance of the model for this application of tomographic imaging.

The paper is organized as follows. In Section 2, we initially establish the uniqueness of the solution to a weighted Total Variation regularization model, followed by an exposition of our approach for determining the weights. Subsequently, we outline the algorithmic aspects in Section 3 and we conduct numerical experiments in Section 4 to evaluate the effectiveness of our proposal across various implementations. Finally, we discuss our approach and set the conclusions in Section 5, whereas we refer to the Appendix A for further theoretical aspects.

2 Space-Variant regularization models

In this Section, we state our regularized model and derive important theoretical results about its convergence to a unique optimal solution.

To simplify the readability of the upcoming results, we introduce here some notations. When not specified, we always assume vectors \mathbf{x} to lie in $\mathcal{X} \subseteq \mathbb{R}^n$, which we assume to be convex. Thus, for any $\mathbf{x}, \mathbf{y} \in \mathcal{X}$, the symbol $\langle \mathbf{x}, \mathbf{y} \rangle$ represents the standard inner product in \mathbb{R}^n . Moreover, if $\mathbf{x}, \mathbf{y} \in \mathbb{R}^n$, we say that $\mathbf{x} \leq \mathbf{y}$ if and only if $x_i \leq y_i$ for any $i = 1, \dots, n$. If $\mathbf{A} \in \mathbb{R}^{m \times n}$ is a linear operator, then \mathbf{A}^T represents the transpose of \mathbf{A} . If $C \subseteq \mathbb{R}^n$, then $\iota_C(\mathbf{x})$ is the characteristic function of C , defined as:

$$\iota_C(\mathbf{x}) = \begin{cases} 0 & \text{if } \mathbf{x} \in C, \\ +\infty & \text{if } \mathbf{x} \notin C. \end{cases} \quad (3)$$

Finally, we define the 2-dimensional discrete gradient operator $\mathbf{D} : \mathbb{R}^n \rightarrow \mathbb{R}^{2n}$, such that:

$$\mathbf{D}\mathbf{x} = \begin{bmatrix} \mathbf{D}_h\mathbf{x} \\ \mathbf{D}_v\mathbf{x} \end{bmatrix} \in \mathbb{R}^{2n}, \quad (4)$$

where $\mathbf{D}_h, \mathbf{D}_v \in \mathbb{R}^{n \times n}$ are the discrete central differences operators associated with the horizontal and vertical derivatives, respectively, and $|\mathbf{D}\mathbf{x}| \in \mathbb{R}^n$ is the gradient-magnitude image of \mathbf{x} , defined as:

$$(|\mathbf{D}\mathbf{x}|)_i = \sqrt{(\mathbf{D}_h\mathbf{x})_i^2 + (\mathbf{D}_v\mathbf{x})_i^2}. \quad (5)$$

Note that, from (4), it holds that $(\mathbf{D}\mathbf{x})_i = (\mathbf{D}_h\mathbf{x})_i$ for $i = 1, \dots, n$, while $(\mathbf{D}\mathbf{x})_i = (\mathbf{D}_v\mathbf{x})_{i-n}$ for $i = n+1, \dots, 2n$.

2.1 Regularization based on Total Variation

Space-variant (or adaptive) regularization functions, which operate distinctively within each pixel of the image, have been proposed in the literature, primarily grounded in the Total Variation approach. The popular isotropic Total Variation operator $TV(\mathbf{x})$ is the Rudin, Osher, Fatemi prior [27] defined as:

$$TV(\mathbf{x}) = \|\mathbf{D}\mathbf{x}\|_{2,1} := \sum_{i=1}^n \sqrt{(\mathbf{D}_h\mathbf{x})_i^2 + (\mathbf{D}_v\mathbf{x})_i^2}. \quad (6)$$

In a recent review by [26], the authors demonstrate the efficacy of space-variant TV-based regularization in addressing the limitations of TV in characterizing local features. Indeed, a widely employed technique to derive space-variant models involves weighting the regularization function pixel-wise. They suggest various sparsifying regularization functions with weights derived from a Bayesian interpretation of the model. In other papers, these weights are typically determined based on either an estimation of the data noise [18, 19, 3, 6], by an assessment of the image scaling [17, 10] or by means of specifically trained neural networks [11]. An alternative approach entails utilizing diverse measures of the image gradient, as exemplified in the Total p-Variation (TpV) regularization method, which typically is:

$$\|\mathbf{D}\mathbf{x}\|_{2,p}^p := \sum_{i=1}^n \left(\sqrt{(\mathbf{D}_h\mathbf{x})_i^2 + (\mathbf{D}_v\mathbf{x})_i^2} \right)^p \quad (7)$$

with $0 < p < 1$. In this scenario, the parameter p can be adapted for each pixel of the image [10, 9].

All the referenced papers employ regularization techniques to address denoising and deblurring problems, wherein the observed image (datum) and the reconstructed image (solution) belong to the same space. However, our application differs in that the data (sinogram) resides in a lower-dimensional space of the solution; thus, the noise present in the sinogram varies significantly from the noise inherent in the reconstructed image. Indeed, streaking artifacts also impact the reconstructions, originating from the sparsity of the views. Given that several of the referenced algorithms adjust adaptive weights at each iteration of the solver, leading to heightened computational overhead, they are unsuitable for the application under consideration, where optimizing execution time is paramount for practical purposes.

For these reasons, we propose a new space-variant approach wherein pixel-dependent weights are customized to eliminate noise and streaking artifacts, remaining constant throughout all iterations of the solver. In our variational model (2), the space-variant regularizer $\mathcal{R}(\mathbf{x}) = TV_{\mathbf{w}}(\mathbf{x})$ is defined as:

$$TV_{\mathbf{w}}(\mathbf{x}) := \sum_{i=1}^n w_i \sqrt{(\mathbf{D}_h\mathbf{x})_i^2 + (\mathbf{D}_v\mathbf{x})_i^2} = \|\mathbf{w} \odot |\mathbf{D}\mathbf{x}|\|_1, \quad (8)$$

where $\mathbf{w} = (w_1, \dots, w_n) \in \mathbb{R}^n$ is the vector of weights, and \odot is the element-wise product.

2.2 Uniqueness of the solution

In this Section we establish the existence and uniqueness of the solution of problem (2) when $\mathcal{F}(\mathbf{x}, \mathbf{y}^\delta) = \frac{1}{2} \|\mathbf{K}\mathbf{x} - \mathbf{y}^\delta\|_2^2$ and $\mathbb{R}(x) = TV_w(x)$. To accomplish this, we initially focus on demonstrating the case where the regularization function $\mathcal{R}(\mathbf{x})$ corresponds to the TV prior defined in (6). In the following, as it is common in imaging science, we will always refer to \mathcal{X} as the non-negative subspace $\mathcal{X} = \{\mathbf{x} \in \mathbb{R}^n; \mathbf{x}_i \geq \mathbf{0}, \forall i = 1, \dots, n\}$ of \mathbb{R}^n .

In this setting, proving the existence of (possibly many) solutions to the problem is trivial, as the objective function is convex on the convex feasible set \mathcal{X} .

On the contrary, the uniqueness of the optimal solution needs to be investigated more carefully and it passes through some preliminary propositions [20]. In this Section, we denote as $\mathcal{J}(\mathbf{x}) := \mathcal{J}(\mathbf{x}, \mathbf{y}^\delta)$ when the explicit dependence on \mathbf{y}^δ is not relevant. Moreover, we denote as $\mathcal{J}^* = \min_{\mathbf{x} \in \mathcal{X}} \mathcal{J}(\mathbf{x})$, whereas $\mathcal{M} := \{\mathbf{x} \in \mathcal{X} | \mathcal{J}(\mathbf{x}) = \mathcal{J}^*\}$ represents the set of the global minimizers, which is not empty since \mathcal{J} is convex and coercive. We can now state the first important results.

Proposition 1. *For any $\mathbf{x}_1, \mathbf{x}_2 \in \mathbb{R}^n$, it holds:*

$$\mathcal{J}\left(\frac{\mathbf{x}_1 + \mathbf{x}_2}{2}\right) \leq \frac{1}{2} (\mathcal{J}(\mathbf{x}_1) + \mathcal{J}(\mathbf{x}_2)) - \frac{1}{8} \|\mathbf{K}\mathbf{x}_1 - \mathbf{K}\mathbf{x}_2\|_2^2.$$

Proof. The proof is a simple algebraic manipulation of the objective function. Indeed, since $TV(\mathbf{x}) = \|\mathbf{D}\mathbf{x}\|_{2,1}$ is a norm, by the triangular inequality we get:

$$\begin{aligned} \mathcal{J}\left(\frac{\mathbf{x}_1 + \mathbf{x}_2}{2}\right) &= \frac{1}{2} \left\| \mathbf{K}\left(\frac{\mathbf{x}_1 + \mathbf{x}_2}{2}\right) - \mathbf{y}^\delta \right\|_2^2 + \lambda \mathcal{R}\left(\frac{\mathbf{x}_1 + \mathbf{x}_2}{2}\right) \\ &\leq \frac{1}{2} \left\| \mathbf{K}\left(\frac{\mathbf{x}_1 + \mathbf{x}_2}{2}\right) - \mathbf{y}^\delta \right\|_2^2 + \frac{\lambda}{2} (\mathcal{R}(\mathbf{x}_1) + \mathcal{R}(\mathbf{x}_2)). \end{aligned}$$

Moreover, the linearity of \mathbf{K} gives:

$$\begin{aligned} \frac{1}{2} \left\| \mathbf{K}\left(\frac{\mathbf{x}_1 + \mathbf{x}_2}{2}\right) - \mathbf{y}^\delta \right\|_2^2 &= \frac{1}{2} \left\| \frac{\mathbf{K}\mathbf{x}_1 + \mathbf{K}\mathbf{x}_2 - 2\mathbf{y}^\delta}{2} \right\|_2^2 \\ &= \frac{1}{8} \left\| (\mathbf{K}\mathbf{x}_1 - \mathbf{y}^\delta) + (\mathbf{K}\mathbf{x}_2 - \mathbf{y}^\delta) \right\|_2^2 \\ &= \frac{1}{8} \left(\|\mathbf{K}\mathbf{x}_1 - \mathbf{y}^\delta\|_2^2 + \|\mathbf{K}\mathbf{x}_2 - \mathbf{y}^\delta\|_2^2 + 2\langle \mathbf{K}\mathbf{x}_1 - \mathbf{y}^\delta, \mathbf{K}\mathbf{x}_2 - \mathbf{y}^\delta \rangle \right). \end{aligned}$$

Note that, by the bilinearity of the scalar product:

$$\langle \mathbf{K}\mathbf{x}_1 - \mathbf{y}^\delta, \mathbf{K}\mathbf{x}_2 - \mathbf{y}^\delta \rangle = \langle \mathbf{K}\mathbf{x}_1, \mathbf{K}\mathbf{x}_2 \rangle + \langle \mathbf{y}^\delta, \mathbf{y}^\delta \rangle - \langle \mathbf{K}\mathbf{x}_1, \mathbf{y}^\delta \rangle - \langle \mathbf{K}\mathbf{x}_2, \mathbf{y}^\delta \rangle.$$

Now we can complete the square of $\langle \mathbf{K}\mathbf{x}_1, \mathbf{K}\mathbf{x}_2 \rangle$, $\langle \mathbf{K}\mathbf{x}_1, \mathbf{y}^\delta \rangle$, and $\langle \mathbf{K}\mathbf{x}_2, \mathbf{y}^\delta \rangle$ by adding and subtracting $\frac{\|\mathbf{K}\mathbf{x}_1\|_2^2}{2}$ and $\frac{\|\mathbf{K}\mathbf{x}_2\|_2^2}{2}$ to obtain:

$$2\langle \mathbf{K}\mathbf{x}_1 - \mathbf{y}^\delta, \mathbf{K}\mathbf{x}_2 - \mathbf{y}^\delta \rangle = -\|\mathbf{K}\mathbf{x}_1 - \mathbf{K}\mathbf{x}_2\|_2^2 + \|\mathbf{K}\mathbf{x}_1 - \mathbf{y}^\delta\|_2^2 + \|\mathbf{K}\mathbf{x}_2 - \mathbf{y}^\delta\|_2^2.$$

Substituting this value in the inequality above gives:

$$\begin{aligned} \mathcal{J}\left(\frac{\mathbf{x}_1 + \mathbf{x}_2}{2}\right) &\leq \frac{1}{2} \left\| \mathbf{K}\left(\frac{\mathbf{x}_1 + \mathbf{x}_2}{2}\right) - \mathbf{y}^\delta \right\|_2^2 + \frac{\lambda}{2} (\mathcal{R}(\mathbf{x}_1) + \mathcal{R}(\mathbf{x}_2)) \\ &= \frac{1}{2} \left(\frac{1}{2} \|\mathbf{K}\mathbf{x}_1 - \mathbf{y}^\delta\|_2^2 + \frac{1}{2} \|\mathbf{K}\mathbf{x}_2 - \mathbf{y}^\delta\|_2^2 - \frac{1}{4} \|\mathbf{K}\mathbf{x}_1 - \mathbf{K}\mathbf{x}_2\|_2^2 \right) + \frac{\lambda}{2} (\mathcal{R}(\mathbf{x}_1) + \mathcal{R}(\mathbf{x}_2)). \end{aligned}$$

Grouping together the fidelities with the corresponding regularization terms to form \mathcal{J} , we finally obtain:

$$\mathcal{J}\left(\frac{\mathbf{x}_1 + \mathbf{x}_2}{2}\right) \leq \frac{1}{2} (\mathcal{J}(\mathbf{x}_1) + \mathcal{J}(\mathbf{x}_2)) - \frac{1}{8} \|\mathbf{K}\mathbf{x}_1 - \mathbf{K}\mathbf{x}_2\|_2^2.$$

□

An important consequence of this Proposition is that the difference of any two minimizers of $\mathcal{J}(\mathbf{x})$ must lie in the kernel of \mathbf{K} .

Proposition 2. For any $\mathbf{x}_1, \mathbf{x}_2 \in \mathcal{M}$, it holds $\mathbf{x}_1 - \mathbf{x}_2 \in \ker(\mathbf{K})$.

Proof. Since $\mathcal{J}(\mathbf{x})$ is convex, the set \mathcal{M} of its minima is convex. Consequently, if both $\mathbf{x}_1, \mathbf{x}_2 \in \mathcal{M}$, also $\frac{\mathbf{x}_1 + \mathbf{x}_2}{2} \in \mathcal{M}$. However, by Proposition 1, we get:

$$\mathcal{J}\left(\frac{\mathbf{x}_1 + \mathbf{x}_2}{2}\right) \leq \frac{1}{2}(\mathcal{J}(\mathbf{x}_1) + \mathcal{J}(\mathbf{x}_2)) - \frac{1}{8}\|\mathbf{K}\mathbf{x}_1 - \mathbf{K}\mathbf{x}_2\|_2^2,$$

where:

$$\mathcal{J}(\mathbf{x}_1) = \mathcal{J}(\mathbf{x}_2) = \mathcal{J}\left(\frac{\mathbf{x}_1 + \mathbf{x}_2}{2}\right) = \mathcal{J}^*.$$

Consequently, we get:

$$\mathcal{J}^* \leq \frac{1}{2}(\mathcal{J}^* + \mathcal{J}^*) - \frac{1}{4}\|\mathbf{K}\mathbf{x}_1 - \mathbf{K}\mathbf{x}_2\|_2^2 = \mathcal{J}^* - \frac{1}{8}\|\mathbf{K}\mathbf{x}_1 - \mathbf{K}\mathbf{x}_2\|_2^2$$

and it holds if and only if $\|\mathbf{K}\mathbf{x}_1 - \mathbf{K}\mathbf{x}_2\|_2^2 = 0$, i.e. if $\mathbf{K}(\mathbf{x}_1 - \mathbf{x}_2) = \mathbf{0}$ which concludes the proof. \square

Note that, since \mathbf{K} is undersampled by assumption, $\ker(\mathbf{K})$ is not trivial in general, which implies that Proposition 2 is not sufficient to prove that the solution of (2) is unique. However, Proposition 2 implies an interesting property of the TV regularizer.

Proposition 3. For any $\mathbf{x}_1, \mathbf{x}_2 \in \mathcal{M}$, it holds $\mathcal{R}(\mathbf{x}_1) = \mathcal{R}(\mathbf{x}_2)$.

Proof. Since we assume $\mathbf{x}_1, \mathbf{x}_2 \in \mathcal{M}$, Proposition 2 suggests that $\mathbf{x}_1 - \mathbf{x}_2 \in \ker(\mathbf{K})$, i.e. $\mathbf{K}\mathbf{x}_1 = \mathbf{K}\mathbf{x}_2$ and it implies that $\mathcal{F}(\mathbf{x}_1, \mathbf{y}^\delta) = \mathcal{F}(\mathbf{x}_2, \mathbf{y}^\delta)$. Moreover, by convexity, $\mathcal{J}(\mathbf{x}_1) = \mathcal{J}(\mathbf{x}_2) = \mathcal{J}^*$, hence the result trivially follows. \square

A last step to prove the uniqueness of the solution to the TV-grounded Problem (2) requires fixing some preliminary notations. Denoting by $I_h = \{1, \dots, n\}$ and $I_v = \{n+1, \dots, 2n\}$ the sets of indices of $\mathbf{D}\mathbf{x}$ related to the horizontal and vertical derivatives of \mathbf{x} , the operator $\hat{\mathbf{D}}\mathbf{x} : \mathbb{R}^n \rightarrow \mathbb{R}^{2n}$ is defined as follows:

$$\forall i \in I_h, \quad (\hat{\mathbf{D}}\mathbf{x})_i = (\hat{\mathbf{D}}_h\mathbf{x})_i := \begin{cases} \frac{(\mathbf{D}_h\mathbf{x})_i}{(|\mathbf{D}\mathbf{x}|)_i} & \text{if } (|\mathbf{D}\mathbf{x}|)_i \neq 0, \\ \frac{1}{2} & \text{otherwise,} \end{cases} \quad (9)$$

$$\forall i \in I_v, \quad (\hat{\mathbf{D}}\mathbf{x})_i = (\hat{\mathbf{D}}_v\mathbf{x})_{i-n} := \begin{cases} \frac{(\mathbf{D}_v\mathbf{x})_{i-n}}{(|\mathbf{D}\mathbf{x}|)_{i-n}} & \text{if } (|\mathbf{D}\mathbf{x}|)_{i-n} \neq 0, \\ \frac{1}{2} & \text{otherwise,} \end{cases} \quad (10)$$

where $(|\mathbf{D}\mathbf{x}|)_i$ is the i -th element of the gradient magnitude of \mathbf{x} , as defined in (5). The importance of $\hat{\mathbf{D}}$ resides in the following property.

Proposition 4. For any $\mathbf{x} \in \mathcal{X}$, it holds $\|\mathbf{D}\mathbf{x}\|_{2,1} = \langle \hat{\mathbf{D}}\mathbf{x}, \mathbf{D}\mathbf{x} \rangle$.

Proof. First of all, by definition, we get:

$$\|\mathbf{D}\mathbf{x}\|_{2,1} = \sum_{i=1}^n (|\mathbf{D}\mathbf{x}|)_i.$$

whereas:

$$\langle \hat{\mathbf{D}}\mathbf{x}, \mathbf{D}\mathbf{x} \rangle = \sum_{i=1}^{2n} (\hat{\mathbf{D}}\mathbf{x})_i (\mathbf{D}\mathbf{x})_i.$$

Note that, for any $i \in I_h$ such that $(|\mathbf{D}\mathbf{x}|)_i \neq 0$ it holds $(\hat{\mathbf{D}}\mathbf{x})_i (\mathbf{D}\mathbf{x})_i = \frac{(\mathbf{D}\mathbf{x})_i^2}{(|\mathbf{D}\mathbf{x}|)_i}$, and similarly $(\hat{\mathbf{D}}\mathbf{x})_i (\mathbf{D}\mathbf{x})_i = \frac{(\mathbf{D}\mathbf{x})_i^2}{(|\mathbf{D}\mathbf{x}|)_{i-n}}$ for any $i \in I_v$ such that $(|\mathbf{D}\mathbf{x}|)_{i-n} \neq 0$. On the contrary, $(\hat{\mathbf{D}}\mathbf{x})_i (\mathbf{D}\mathbf{x})_i = 0$ whenever $(|\mathbf{D}\mathbf{x}|)_i = 0$ for

$i \in I_h$ and whenever $(|\mathbf{D}\mathbf{x}|)_{i-n} = 0$ for $i \in I_v$. Consequently:

$$\begin{aligned} \sum_{i=1}^{2n} (\hat{\mathbf{D}}\mathbf{x})_i (\mathbf{D}\mathbf{x})_i &= \sum_{i:(|\mathbf{D}\mathbf{x}|)_i \neq 0} \frac{(\mathbf{D}\mathbf{x})_i^2}{(|\mathbf{D}\mathbf{x}|)_i} = \sum_{\substack{i \in I_h \\ (|\mathbf{D}\mathbf{x}|)_i \neq 0}} \frac{(\mathbf{D}_h \mathbf{x})_i^2}{(|\mathbf{D}\mathbf{x}|)_i} + \sum_{\substack{i \in I_v \\ (|\mathbf{D}\mathbf{x}|)_{i-n} \neq 0}} \frac{(\mathbf{D}_v \mathbf{x})_{i-n}^2}{(|\mathbf{D}\mathbf{x}|)_{i-n}} \\ &= \sum_{\substack{i \in I_h \\ (|\mathbf{D}\mathbf{x}|)_i \neq 0}} \frac{(\mathbf{D}_h \mathbf{x})_i^2 + (\mathbf{D}_v \mathbf{x})_i^2}{(|\mathbf{D}\mathbf{x}|)_i} = \sum_{\substack{i \in I_h \\ (|\mathbf{D}\mathbf{x}|)_i \neq 0}} \frac{(|\mathbf{D}\mathbf{x}|)_i^2}{(|\mathbf{D}\mathbf{x}|)_i} + \sum_{\substack{i \in I_h \\ (|\mathbf{D}\mathbf{x}|)_i = 0}} (|\mathbf{D}\mathbf{x}|)_i \\ &= \sum_{i=1}^n (|\mathbf{D}\mathbf{x}|)_i = \|\mathbf{D}\mathbf{x}\|_{2,1}, \end{aligned}$$

which concludes the proof. \square

With these tools, we can now prove the last preliminary propositions, which will allow to prove the main result for this Section.

Proposition 5. *Let $\mathbf{x}_1 \in \mathcal{M}$ and $\bar{I} = \{i \in \{1, \dots, n\} \mid (|\mathbf{D}\mathbf{x}_1|)_i = 0\}$. Considering the set $S_1 := \{\mathbf{v} \in \mathbb{R}^n \mid (|\mathbf{D}\mathbf{v}|)_i = 0 \forall i \in \bar{I}\}$. Then S_1 is a vectorial space and $\mathbf{x}_1 \in S_1$.*

Proof. Clearly, $\mathbf{x}_1 \in S_1$ since $(|\mathbf{D}\mathbf{x}_1|)_i = 0$ for any $i \in \bar{I}$. Moreover, $\mathbf{0} \in S_1$ since $(|\mathbf{D}\mathbf{0}|)_i$ equals 0 for any $i = 1, \dots, n$ and in particular for any $i \in \bar{I}$. Now, let $\mathbf{v}, \mathbf{w} \in S_1$ and $\alpha, \beta \in \mathbb{R}$. Then $\mathbf{t} := \alpha\mathbf{v} + \beta\mathbf{w} \in S_1$ since $(|\mathbf{D}\mathbf{t}|)_i = \alpha(|\mathbf{D}\mathbf{v}|)_i + \beta(|\mathbf{D}\mathbf{w}|)_i = 0$ for any $i \in \bar{I}$. This concludes the proof. \square

We can now prove the uniqueness of the solution of an underdetermined inverse problem with TV regularization, with the following Theorem.

Theorem 6 (Unicity theorem). *Let $\mathbf{x}_1 \in \mathcal{M}$ and assume:*

- (i) $\exists \mathbf{z} \in \mathbb{R}^n$ s.t. $\mathbf{D}^T \hat{\mathbf{D}}\mathbf{x}_1 = \mathbf{K}^T \mathbf{z}$,
- (ii) $\ker(\mathbf{K}) \cap S_1 = \{\mathbf{0}\}$.

Then the solution of Problem (2) with $\mathcal{F}(\mathbf{x}, \mathbf{y}^\delta) = \frac{1}{2} \|\mathbf{K}\mathbf{x} - \mathbf{y}^\delta\|_2^2$ and $\mathbb{R}(x) = TV(x)$ is unique, i.e. $\mathcal{M} = \{\mathbf{x}_1\}$.

Proof. Let $\mathbf{x}_1 \in \mathcal{M}$ and we consider $\mathbf{x}_2 \in \mathcal{M}$ to show that necessarily $\mathbf{x}_1 = \mathbf{x}_2$. To this aim, we consider the two complementary cases of $\mathbf{x}_2 \in S_1$ and $\mathbf{x}_2 \notin S_1$.

If $\mathbf{x}_2 \in S_1$, then $\mathbf{x}_1 - \mathbf{x}_2 \in S_1$ as well, since S_1 is a vectorial space by Proposition 5 and it is closed by sum. Moreover, by Proposition 2, $\mathbf{x}_1 - \mathbf{x}_2 \in \ker(\mathbf{K})$. Consequently, for the second assumption of this Theorem, $\mathbf{x}_1 = \mathbf{x}_2$.

If $\mathbf{x}_2 \notin S_1$, there must exist at least an index $i_0 \in \bar{I}$ such that $(|\mathbf{D}\mathbf{x}_2|)_{i_0} \neq 0$. In addition, according to the definition of $\hat{\mathbf{D}}$ given in (9) and (10), $(\mathbf{D}_h \mathbf{x}_1)_{i_0} = (\mathbf{D}_v \mathbf{x}_1)_{i_0} = 0$ and $(\hat{\mathbf{D}}_h \mathbf{x}_1)_{i_0} = (\hat{\mathbf{D}}_v \mathbf{x}_1)_{i_0} = \frac{1}{2}$. Now, recalling the result in Proposition 4:

$$\mathcal{R}(\mathbf{x}_1) = \|\mathbf{D}\mathbf{x}_1\|_{2,1} = \langle \hat{\mathbf{D}}\mathbf{x}_1, \mathbf{D}\mathbf{x}_1 \rangle,$$

and by means of adjoint matrix, if $\mathbf{z} \in \mathbb{R}^n$ is the variable defined by the first hypothesis:

$$\langle \hat{\mathbf{D}}\mathbf{x}_1, \mathbf{D}\mathbf{x}_1 \rangle = \langle \mathbf{D}^T \hat{\mathbf{D}}\mathbf{x}_1, \mathbf{x}_1 \rangle = \langle \mathbf{K}^T \mathbf{z}, \mathbf{x}_1 \rangle.$$

Thus, by Propositions 2 and 4, we get:

$$\begin{aligned} \mathcal{R}(\mathbf{x}_1) &= \langle \mathbf{K}^T \mathbf{z}, \mathbf{x}_1 \rangle = \langle \mathbf{z}, \mathbf{K}\mathbf{x}_1 \rangle = \langle \mathbf{z}, \mathbf{K}\mathbf{x}_2 \rangle = \langle \mathbf{K}^T \mathbf{z}, \mathbf{x}_2 \rangle \\ &= \langle \mathbf{D}^T \hat{\mathbf{D}}\mathbf{x}_1, \mathbf{x}_2 \rangle = \langle \hat{\mathbf{D}}\mathbf{x}_1, \mathbf{D}\mathbf{x}_2 \rangle. \end{aligned}$$

In addition, we can derive the following inequality:

$$\begin{aligned} \langle \hat{\mathbf{D}}\mathbf{x}_1, \mathbf{D}\mathbf{x}_2 \rangle &= \sum_{i=1}^{2n} (\hat{\mathbf{D}}\mathbf{x}_1)_i (\mathbf{D}\mathbf{x}_2)_i \leq \sum_{i=1}^n \sqrt{(\hat{\mathbf{D}}_h \mathbf{x}_1)_i^2 + (\hat{\mathbf{D}}_v \mathbf{x}_1)_i^2} \cdot \sqrt{(\mathbf{D}_h \mathbf{x}_2)_i^2 + (\mathbf{D}_v \mathbf{x}_2)_i^2} \\ &= \sum_{i=1}^n \sqrt{(\hat{\mathbf{D}}_h \mathbf{x}_1)_i^2 + (\hat{\mathbf{D}}_v \mathbf{x}_1)_i^2} \cdot (|\mathbf{D}\mathbf{x}_2|)_i, \end{aligned}$$

for the Cauchy-Schwartz inequality applied onto the 2-dimensional vectors $[(\hat{\mathbf{D}}_h \mathbf{x}_1)_i, (\hat{\mathbf{D}}_v \mathbf{x}_1)_i]$ and $[(\mathbf{D}_h \mathbf{x}_2)_i, (\mathbf{D}_v \mathbf{x}_2)_i]$, for all the indexes i separately. To conclude, note that by definition of $\hat{\mathbf{D}}$, it holds:

$$\sqrt{(\hat{\mathbf{D}}_h \mathbf{x}_1)_i^2 + (\hat{\mathbf{D}}_v \mathbf{x}_1)_i^2} = \begin{cases} 1 & \text{if } (|\mathbf{D} \mathbf{x}_1|)_i \neq 0, \\ \frac{1}{\sqrt{2}} & \text{if } (|\mathbf{D} \mathbf{x}_1|)_i = 0. \end{cases} \quad (11)$$

Consequently,

$$\begin{aligned} & \sum_{i=1}^n \sqrt{(\hat{\mathbf{D}}_h \mathbf{x}_1)_i^2 + (\hat{\mathbf{D}}_v \mathbf{x}_1)_i^2} (|\mathbf{D} \mathbf{x}_2|)_i \\ &= \sum_{i \in \{1, \dots, n\} \setminus \{i_0\}} \sqrt{(\hat{\mathbf{D}}_h \mathbf{x}_1)_i^2 + (\hat{\mathbf{D}}_v \mathbf{x}_1)_i^2} (|\mathbf{D} \mathbf{x}_2|)_i + \sqrt{(\hat{\mathbf{D}}_h \mathbf{x}_1)_{i_0}^2 + (\hat{\mathbf{D}}_v \mathbf{x}_1)_{i_0}^2} (|\mathbf{D} \mathbf{x}_2|)_{i_0} \\ &\leq \sum_{i \in \{1, \dots, n\} \setminus \{i_0\}} (|\mathbf{D} \mathbf{x}_2|)_i + \sqrt{(\hat{\mathbf{D}}_h \mathbf{x}_1)_{i_0}^2 + (\hat{\mathbf{D}}_v \mathbf{x}_1)_{i_0}^2} (|\mathbf{D} \mathbf{x}_2|)_{i_0} \\ &< \sum_{i \in \{1, \dots, n\} \setminus \{i_0\}} (|\mathbf{D} \mathbf{x}_2|)_i + (|\mathbf{D} \mathbf{x}_2|)_{i_0} = \sum_{i=1}^n (|\mathbf{D} \mathbf{x}_2|)_i = \|\mathbf{D} \mathbf{x}_2\|_{2,1} = \mathcal{R}(\mathbf{x}_2). \end{aligned}$$

Bringing together the previous inequalities, we have demonstrated that $\mathcal{R}(\mathbf{x}_1) < \mathcal{R}(\mathbf{x}_2)$, which is a contradiction with Proposition 3, where we proved that if $\mathbf{x}_1, \mathbf{x}_2 \in \mathcal{M}$, then $\mathcal{R}(\mathbf{x}_1) = \mathcal{R}(\mathbf{x}_2)$. Thus, every element of \mathcal{M} must be in S_1 and it implies that $\mathcal{M} = \{\mathbf{x}_1\}$. \square

Note that the first condition of Theorem 6 is satisfied whenever $\mathbf{D}^T \hat{\mathbf{D}} \mathbf{x}_1 \in \text{Rg}(\mathbf{K}^T)$, the range of \mathbf{K}^T . We recall that $\text{Rg}(\mathbf{K}^T) = \ker(\mathbf{K})^\perp$, whose dimension depends on the number of CT acquisitions performed by \mathbf{K} . Consequently, Theorem 6 implies that, whenever the number of acquisitions is sufficiently large, then the solution to Problem (2) is unique.

In addition, Theorem 6 can be simply extended to prove the uniqueness of the solution of any space-variant TV regularized model, i.e. when $\mathbb{R}(x) = \text{TV}_w(x)$. To achieve this, consider the matrix \mathcal{W} defined as a $2n \times 2n$ diagonal matrix with two equal diagonal blocks of size $n \times n$, where the elements $(\mathbf{w})_i$ reside on the diagonal. Observing that:

$$\|\mathbf{w} \odot |\mathbf{D} \mathbf{x}|\|_1 = \|\mathcal{W} \mathbf{D} \mathbf{x}\|_{2,1},$$

we can state the following Corollary.

Corollary 7. *Replacing \mathbf{D} with $\mathcal{W} \mathbf{D}$ in the assumptions of Theorem 6, then the problem:*

$$\min_{\mathbf{x} \in \mathcal{X}} \mathcal{J}(\mathbf{x}, \mathbf{y}^\delta) := \frac{1}{2} \|\mathbf{K} \mathbf{x} - \mathbf{y}^\delta\|_2^2 + \lambda \|\mathbf{w} \odot |\mathbf{D} \mathbf{x}|\|_1 \quad (12)$$

always admits a unique solution in $\mathcal{X} = \{\mathbf{x} \in \mathbb{R}^n; \mathbf{x}_i \geq \mathbf{0} \forall i = 1, \dots, n\}$.

The proof is trivial by replacing \mathbf{D} with $\mathcal{W} \mathbf{D}$ in the proof of Theorem 6.

In the following, we assume that these hypotheses are satisfied by our operator \mathbf{K} .

2.3 On the choice of the weights

In this Section we focus on the selection of the weights \mathbf{w} in the TV model (12), which is a matter of high delicacy. Ideally, w_i should be small if the corresponding pixel \mathbf{x}_i of image to be restored lies either close to an edge of a low-contrast region or on a small detail, so that the regularization strength on that pixel is moderate and the fidelity term recovers the information provided in the data \mathbf{y}^δ . Similarly, to maximize the regularization effect, w_i should be high on large and uniform regions of \mathbf{x} so that the emerging of streaking artifacts and the noise propagation get removed or hindered.

To determine the weights \mathbf{w} , we drew inspiration from the paper [28], where the authors successfully utilize the TpV regularization (7) in few-view CT. This regularization method efficiently promotes sparsity in the gradient domain and mitigates the undesired blurring effects often associated with Total Variation regularization, particularly on critical details and edges. In particular, we establish the weighting factors motivated by the iterative reweighting ℓ_1 -norm strategy [5, 12], commonly utilized in solving TpV problems, as:

$$\mathbf{w}_\eta(\tilde{\mathbf{x}}) := \left(\frac{\eta}{\sqrt{\eta^2 + |\mathbf{D} \tilde{\mathbf{x}}|^2}} \right)^{1-p}, \quad (13)$$

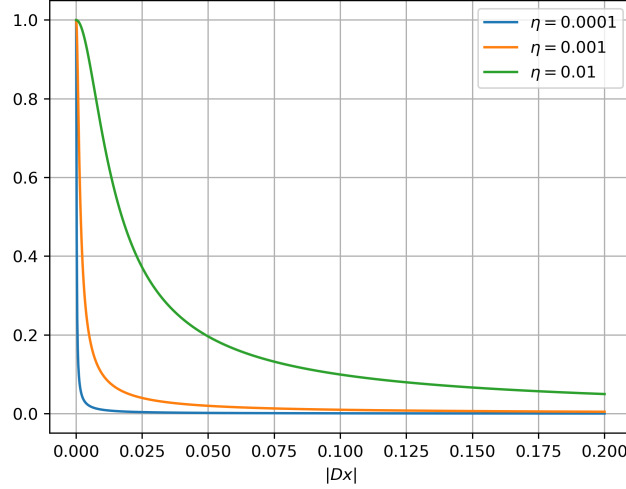


Figure 1: A plot of $(\mathbf{w}_\eta(\tilde{\mathbf{x}}))_i$ for different values of η , over $|\mathbf{D}\tilde{\mathbf{x}}|_i$.

where $\tilde{\mathbf{x}} \in \mathbb{R}^n$ is a suitable image and $\eta \geq 0$ is a scalar parameter.

The following statements serve to elucidate the conceptual underpinnings of our weight parameters, formally.

Proposition 8. For any $\eta > 0$, any $0 < p < 1$, and any $\tilde{\mathbf{x}} \in \mathbb{R}^n$, $(\mathbf{w}_\eta(\tilde{\mathbf{x}}))_i \in (0, 1]$, $\forall i = 1, \dots, n$. Moreover, $(\mathbf{w}_\eta(\tilde{\mathbf{x}}))_i = 1$ on a pixel $i \in 1, \dots, n$ if and only if $|\mathbf{D}\tilde{\mathbf{x}}|_i = 0$.

Proof. Note that, for any $0 < p < 1$, $1 - p > 0$. Consequently,

$$(\mathbf{w}_\eta(\tilde{\mathbf{x}}))_i = \left(\frac{\eta}{\sqrt{\eta^2 + |\mathbf{D}\tilde{\mathbf{x}}|^2}} \right)^{1-p} \in (0, 1] \iff \frac{\eta}{\sqrt{\eta^2 + |\mathbf{D}\tilde{\mathbf{x}}|^2}} \in (0, 1].$$

Moreover, since both η and $\sqrt{\eta^2 + |\mathbf{D}\tilde{\mathbf{x}}|^2}$ are strictly positive, their ratio is necessarily strictly positive. On the other side,

$$\frac{\eta}{\sqrt{\eta^2 + |\mathbf{D}\tilde{\mathbf{x}}|^2}} \leq 1 \iff \eta \leq \sqrt{\eta^2 + |\mathbf{D}\tilde{\mathbf{x}}|^2} \iff |\mathbf{D}\tilde{\mathbf{x}}|^2 \geq 0,$$

which holds for any $\tilde{\mathbf{x}} \in \mathbb{R}^n$, and $|\mathbf{D}\tilde{\mathbf{x}}|_i^2 = 0$ on a pixel i if and only if $|\mathbf{D}\tilde{\mathbf{x}}|_i = 0$. □

Now we observe that whenever $|\mathbf{D}\tilde{\mathbf{x}}|_i = 0$ (i.e., if $\tilde{\mathbf{x}}_i$ is on a flat region), then $(\mathbf{w}_\eta(\tilde{\mathbf{x}}))_i = 1$, and the Total Variation is exactly weighted by λ . Conversely, whenever $|\mathbf{D}\tilde{\mathbf{x}}|_i \gg 0$ (indicating that pixel i is either on an edge or a small detail), then $(\mathbf{w}_\eta(\tilde{\mathbf{x}}))_i < 1$, signifying that the Total Variation regularization is weaker, and the details are preserved. Focusing now on the role of η in the computation of the weights \mathbf{w}_η , Figure 1 shows the value of $(\mathbf{w}_\eta(\tilde{\mathbf{x}}))_i$ at increasing values of $|\mathbf{D}\tilde{\mathbf{x}}|_i$, for different values of $\eta > 0$. It is evident that, for very small values of η , $(\mathbf{w}_\eta(\tilde{\mathbf{x}}))_i$ rapidly decreases to zero (i.e., the solution of the problem is not regularized around pixel i). On the other side, for large values of η , $(\mathbf{w}_\eta(\tilde{\mathbf{x}}))_i$ decreases very slowly as a function of $|\mathbf{D}\tilde{\mathbf{x}}|_i$, which implies that small details will be flattened out. Wrapping up the analysis of weights, we emphasize that since the optimal values of \mathbf{w}_η are linked to the contrasts and the arrangement of details in \mathbf{x}^{GT} , we strive for $|\mathbf{D}\tilde{\mathbf{x}}|$ to closely resemble $|\mathbf{D}\mathbf{x}^{GT}|$, especially near the edges.

To provide a more precise specification on how to derive $\tilde{\mathbf{x}}$ from \mathbf{y}^δ we consider $\Psi : \mathbb{R}^m \rightarrow \mathbb{R}^n$ as a Lipschitz-continuous function that maps \mathbf{y}^δ to an approximate reconstruction $\tilde{\mathbf{x}} = \Psi(\mathbf{y}^\delta)$ of \mathbf{x}^{GT} . In accordance with the nomenclature introduced in [15], we denote such mappings as *reconstructors*.

Hence, given a reconstructor $\Psi : \mathbb{R}^m \rightarrow \mathbb{R}^n$, $\lambda > 0$ and $\eta > 0$, we can formalize the proposed weighted TV model as:

$$\arg \min_{\mathbf{x} \in \mathcal{X}} \frac{1}{2} \|\mathbf{K}\mathbf{x} - \mathbf{y}^\delta\|_2^2 + \lambda \|\mathbf{w}_\eta(\tilde{\mathbf{x}}) \odot |\mathbf{D}\mathbf{x}|\|_1 \quad (14)$$

where $\tilde{\mathbf{x}} = \Psi(\mathbf{y}^\delta)$, the space-variant weights are computed as in Equation (13) and $\mathcal{X} = \{\mathbf{x} \in \mathbb{R}^n; \mathbf{x}_i \geq \mathbf{0}, \forall i = 1, \dots, n\}$, representing the non-negative subspace of \mathbb{R}^n . In the following, we denote the solution of (14) as $\mathbf{x}_{\Psi, \delta}^*$ and we refer to this model as Ψ -W ℓ_1 to remark its reliance on Ψ in the weighted ℓ_1 -norm regularization (as further elaborated upon in Section 2.4).

We have already intuitively observed that \mathbf{x}^{GT} would be a suitable candidate for $\tilde{\mathbf{x}}$. This intuition is further confirmed by the numerical results obtained from simulations (presented in Section 4). Indeed, if we use the ground truth image to compute the space-variant weights, we can achieve highly accurate solutions (that will be referred to as $\mathbf{x}_{GT, \delta}^*$, with a minor notational adaptation).

However, the ground truth images are not available in real cases, hence we need to use a reconstructor working on the noisy data. Under a few assumptions, we can demonstrate that if $|\mathbf{D}\Psi(\mathbf{y}^\delta)|$ provides a good approximation of $|\mathbf{D}\mathbf{x}^{GT}|$, then the solution obtained considering $\mathbf{w}_\eta(\Psi(\mathbf{y}^\delta))$ is a reliable approximation of $\mathbf{x}_{GT, \delta}^*$. To this aim, we need to build a sequence of reconstructors $\Psi_k : \mathbb{R}^m \rightarrow \mathbb{R}^n$ indexed by k , and demonstrate the following theorem.

Theorem 9. *Given $\delta > 0$, let $\{\Psi_k\}_{k \in \mathbb{N}}$ be a sequence of reconstructors such that:*

$$\lim_{k \rightarrow \infty} \|\mathbf{D}\Psi_k(\mathbf{y}^\delta) - \mathbf{D}\mathbf{x}^{GT}\|_1 = 0, \quad \forall \mathbf{y}^\delta = \mathbf{K}\mathbf{x}^{GT} + \mathbf{e}, \|\mathbf{e}\|_2 \leq \delta,$$

then:

$$\lim_{k \rightarrow \infty} \|\mathbf{x}_{\Psi_k, \delta}^* - \mathbf{x}_{GT, \delta}^*\|_1 = 0.$$

The verification of this theorem necessitates numerous observations, the proofs of which, along with the theorem's proof itself, are meticulously expounded in the Appendix A. This organizational choice is made to uphold the overall readability and fluidity of the entire manuscript.

At last, we observe that the above theorem leads to the following result, straightforwardly.

Corollary 10. *Given $\delta > 0$, let $\{\Psi_k\}_{k \in \mathbb{N}}$ be a sequence of reconstructor such that:*

$$\lim_{k \rightarrow \infty} \|\Psi_k(\mathbf{y}^\delta) - \mathbf{x}^{GT}\|_1 = 0, \quad \forall \mathbf{y}^\delta = \mathbf{K}\mathbf{x}^{GT} + \mathbf{e}, \|\mathbf{e}\|_2 \leq \delta,$$

then:

$$\lim_{k \rightarrow \infty} \|\mathbf{x}_{\Psi_k, \delta}^* - \mathbf{x}_{GT, \delta}^*\|_1 = 0.$$

The Corollary suggests that if we can fix a reconstructor whose output is sufficiently close to \mathbf{x}^{GT} for any noisy datum, the optimal images $\mathbf{x}_{\Psi_k, \delta}^*$ and $\mathbf{x}_{GT, \delta}^*$ (computed with the respective weights) will be sufficiently close to each other.

2.4 Proposed Ψ reconstructors

We can now propose various possible choices to define the reconstructor $\Psi(\mathbf{y}^\delta)$ and compute $\tilde{\mathbf{x}}$ from the sinogram \mathbf{y}^δ .

Dealing with tomographic imaging from X-ray measurements, a simple yet fast reconstructor is the Filtered Back Projection (FBP) solver [21]. As an analytical algorithm, it operates by applying a filter to the back-projected data, disregarding the inverse problem formulation of the imaging task. Even if FBP may not address all reconstruction challenges, its speed and simplicity make it a pragmatic choice for many medical imaging scenarios, particularly when balancing computational resources and reconstruction quality is essential.

A further option is setting $\Psi(\mathbf{y}^\delta)$ as an early-stopped variational solver. For example, if we still consider the global TV regularization (6) and stop the iterative algorithm for the solution of the corresponding problem (2) according to computational constraints. While in few-view CT the FBP solution is typically characterized by neat details but also by noise and streaking artifacts, the solution computed by an early stopped TV solver is expected to be a blurred version of the ground truth image, with moderate few-view-caused artifacts. However, we observe that these reconstructors can only provide images approximating \mathbf{x}^{GT} in a classical interpretation.

Another method entails the use of a composition of two reconstructors. We can in fact define $\Psi(\mathbf{y}^\delta) = \Psi_2(\Psi_1(\mathbf{y}^\delta))$, where $\Psi_1(\mathbf{y}^\delta)$ can be one of the previously described reconstructors applied to map the data \mathbf{y}^δ to the image domain, whereas $\Psi_2 : \mathbb{R}^n \rightarrow \mathbb{R}^n$ is designed to enhance the quality of $\Psi_1(\mathbf{y}^\delta)$. In Figure 2, we visually illustrate the contrast between the current and the previous methods for the establishing of Ψ in the Ψ -W ℓ_1 model.

In our specific case, we have chosen Ψ_2 to be a neural network (NN). As extensively documented in the literature, NNs possess the capability to execute efficient image-processing computations through pre-trained deep architectures, offering the flexibility to estimate various image transformations, such as the image gradients [22, 7] or the image

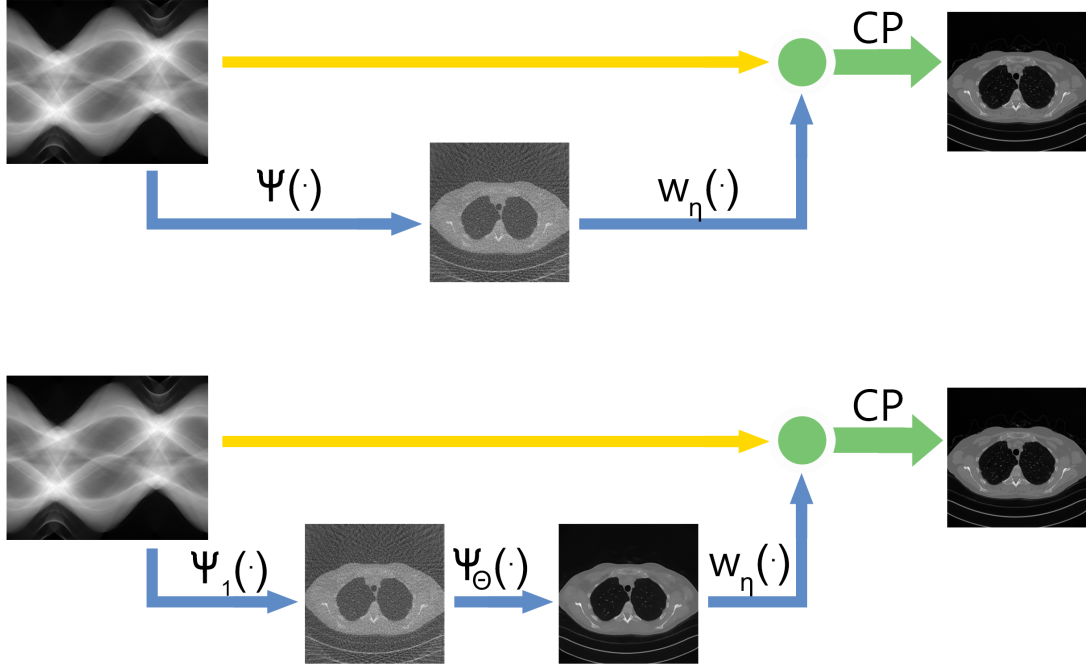


Figure 2: Visual depictions of the proposed Ψ - $W\ell_1$ method, illustrating the key computational steps of our proposal, spanning from the sinogram to the final reconstruction. On the top, the scenario where Ψ is implemented by a single solver; on the bottom, the case where it is formed through a composition of two functions.

shearlets coefficients [4]. However, it is crucial to note that the accuracy of NN reconstructors is contingent upon the quality of the training samples and a considerable computational effort is required during their offline training phase. It is noteworthy that, in the context of medical imaging, the collection of data from the same clinical device allows for the construction of a coherent dataset for training a network. Therefore, we can presume the availability of the training set \mathcal{D} , constituted by M couples $(\mathbf{x}_j^{GT}, \Psi_1(\mathbf{y}_j^\delta))$ of high-quality reconstructed images \mathbf{x}_j^{GT} (to be used as ground truth images) and the corresponding low-quality reconstructions $\Psi_1(\mathbf{y}_j^\delta)$, for all $j = 1, \dots, M$.

We utilize in our experiments the renowned Residual U-Net architecture as described in [24, 14]. A neural network-based reconstructor Ψ_2 can be seen as a Θ parameter-dependent solver, where Θ represents the high-dimensional vector of the NN inner weights; therefore we will denote it as Ψ_Θ in the following. To set these weights, we need to train the network having established a loss function to be minimized. Inspired by the convergence results in Theorem 9 and Corollary 10 where we respectively assume that $|\mathbf{D}\Psi_k(\mathbf{y}^\delta)| \rightarrow |\mathbf{D}\mathbf{x}^{GT}|$ and $\Psi_k(\mathbf{y}^\delta) \rightarrow \mathbf{x}^{GT}$ for $k \rightarrow \infty$, we have designed a loss function such that each $\Psi_\Theta(\Psi_1(\mathbf{y}_j^\delta))$ image approximates not only the ground truth one but also the magnitude images $|\mathbf{D}\mathbf{x}_j^{GT}|$. To this aim, inspired by the regularization technique proposed in [2], we train Ψ_Θ with the *elastic loss*:

$$\Theta^* \in \arg \min_{\Theta} \sum_{j=1}^M \alpha \| |\mathbf{D}\mathbf{x}_j^{GT}| - |\mathbf{D}\Psi_\Theta(\mathbf{y}_j^\delta)| \|_2^2 + (1 - \alpha) \| \mathbf{x}_j^{GT} - \Psi_\Theta(\mathbf{y}_j^\delta) \|_2^2 \quad (15)$$

where $\alpha \in [0, 1]$. Setting $\alpha = 0$ yields a network aimed at achieving the best image approximation, whereas $\alpha = 1$ directs the training process to focus solely on learning gradient images. We anticipate that, in our experimental setting, we will consider $\alpha = \{0, 0.5, 1\}$ to test the effectiveness of the elastic loss in these extreme α values as well as in its central elastic coefficient. In addition, we will use Ψ_1 as the FBP algorithm, to get a comprehensive reconstructing framework of very fast execution. As training samples, we use $M=3305$ couples $(\mathbf{x}_j^{GT}, \Psi_1(\mathbf{y}_j^\delta))$ of real chest images extracted from the Low Dose CT Grand Challenge data set by the Mayo Clinic [23]. They are 256×256 pixel resolution and are normalized in the unitary interval. We perform 50 epochs with Adam optimizer with a learning rate equal to 10^{-3} and $\beta_1 = 0.9$, $\beta_2 = 0.9999$ to complete the training phase.

3 Chambolle-Pock algorithm

To solve the optimization problem (14), we consider the Chambolle-Pock (CP) algorithm [8], that is a popular iterative method used to solve the TV-regularized inverse problem [25, 28] in few-view CT. In its original formulation, it can be employed to minimize an objective function of the form:

$$\min_{\mathbf{x} \in \mathbb{R}^n} F(\mathbf{M}\mathbf{x}) + G(\mathbf{x}), \quad (16)$$

where both F and G are real-valued, proper, convex, lower semi-continuous functions and \mathbf{M} is a linear operator from \mathbb{R}^n to \mathbb{R}^s . Note that there are no constraints on the smoothness of either F and G ; therefore, the method can be applied to our problem by setting:

$$\begin{cases} G(\mathbf{x}) = \iota_{\mathcal{X}}(\mathbf{x}), \\ F(\mathbf{M}\mathbf{x}) = \mathcal{J}_{\Psi}(\mathbf{x}, \mathbf{y}^\delta) = \frac{1}{2} \|\mathbf{K}\mathbf{x} - \mathbf{y}^\delta\|_2^2 + \lambda \|\mathbf{w}_\eta(\tilde{\mathbf{x}}) \odot \mathbf{D}\mathbf{x}\|_1, \end{cases} \quad (17)$$

where $\iota_{\mathcal{X}}(\mathbf{x})$ is the indicator function of the feasible set \mathcal{X} . As already stated, we consider \mathcal{X} as the non-negative subspace of \mathbb{R}^n .

To apply the CP method to our problem, we define the linear operator $\mathbf{M} \in \mathbb{R}^{s \times n}$ by concatenating row-wise \mathbf{K} and \mathbf{D} , namely $\mathbf{M} = [\mathbf{K}; \mathbf{D}]$ and $s = (m + 2n)$. The CP algorithm considers the primal-dual formulation of (16), that reads:

$$\min_{\mathbf{x} \in \mathbb{R}^n} \max_{\mathbf{z} \in \mathbb{R}^{m+2n}} \mathbf{z}^T \mathbf{M}\mathbf{x} + G(\mathbf{x}) - F^*(\mathbf{z}), \quad (18)$$

where F^* is the convex conjugate of F [1], defined as:

$$F^*(\mathbf{z}^*) := \sup_{\mathbf{z} \in \mathbb{R}^{m+2n}} \{ \mathbf{z}^T \mathbf{z}^* - F(\mathbf{z}) \}. \quad (19)$$

Given a starting guess for both the primal variable $\mathbf{x}^{(0)}$ and the dual variable $\mathbf{z}^{(0)}$, the update rule is the following:

$$\begin{cases} \mathbf{z}^{(k+1)} = \text{prox}_{\sigma F^*}(\mathbf{z}^{(k)} + \sigma \mathbf{M}\bar{\mathbf{x}}^{(k)}), \\ \mathbf{x}^{(k+1)} = \text{prox}_{\tau G}(\mathbf{x}^{(k)} - \tau \mathbf{M}^T \mathbf{z}^{(k+1)}), \\ \bar{\mathbf{x}}^{(k+1)} = \mathbf{x}^{(k+1)} + \beta (\mathbf{x}^{(k+1)} - \mathbf{x}^{(k)}), \end{cases} \quad (20)$$

where $\bar{\mathbf{x}}^{(0)} = \mathbf{0}$, $\beta \in [0, 1]$ is a parameter that we set equal to 1 in the experiments, while $\sigma > 0$, $\tau > 0$ are computed as $\sigma = \tau \approx \frac{1}{\|\mathbf{M}\|_2}$. A reliable approximation of $\|\mathbf{M}\|_2$ can be computed by means of the power method [13].

Focusing on $G(\mathbf{x})$, its proximal operator corresponds to the projection \mathcal{P}_+ over the non-negative subspace \mathcal{X} . Consequently the updating rule of the primal variable $\mathbf{x}^{(k)}$ becomes:

$$\mathbf{x}^{(k+1)} = \mathcal{P}_+(\mathbf{x}^{(k)} - \tau \mathbf{M}^T \mathbf{z}^{(k+1)}). \quad (21)$$

The explicit derivation of $\text{prox}_{\sigma F^*}$ requires the introduction of two dual variables, $\mathbf{p} \in \mathbb{R}^m$ and $\mathbf{q} \in \mathbb{R}^{2n}$, such that:

$$F(\mathbf{p}, \mathbf{q}) = \underbrace{\frac{1}{2} \|\mathbf{p} - \mathbf{y}^\delta\|_2^2}_{:= F_1(\mathbf{p})} + \underbrace{\lambda \|\mathbf{w}_\eta(\tilde{\mathbf{x}}) \odot \mathbf{q}\|_1}_{:= F_2(\mathbf{q})}. \quad (22)$$

Denominating $F_1(\mathbf{p}) = \frac{1}{2} \|\mathbf{p} - \mathbf{y}^\delta\|_2^2$, its convex conjugate $F_1^*(\mathbf{p})$ can be easily computed as:

$$F_1^*(\mathbf{p}) = \sup_{\mathbf{p}'} \left\{ \mathbf{p}^T \mathbf{p}' - \frac{1}{2} \|\mathbf{p}' - \mathbf{y}^\delta\|_2^2 \right\} \quad (23)$$

$$= \mathbf{p}^T \mathbf{y}^\delta + \frac{3}{2} \|\mathbf{p}\|_2^2, \quad (24)$$

since the problem defining F_1^* is quadratic in \mathbf{p}' and it can be solved by imposing the optimality condition of null gradient. Consequently, the proximal map of F_1^* gets:

$$\text{prox}_{\sigma F_1^*}(\mathbf{p}) = \arg \min_{\mathbf{p}'} (\mathbf{p}')^T \mathbf{y}^\delta + \frac{3}{2} \|\mathbf{p}'\|_2^2 + \frac{1}{2\sigma} \|\mathbf{p}' - \mathbf{p}\|_2^2 \quad (25)$$

$$= \frac{\mathbf{p} - \sigma \mathbf{y}^\delta}{1 + 3\sigma}. \quad (26)$$

Similarly, calling $F_2(\mathbf{q}) = \lambda \|\mathbf{w}_\eta(\tilde{\mathbf{x}}) \odot \mathbf{q}\|_1$, we derive:

$$F_2^*(\mathbf{q}) = \begin{cases} 0 & \text{if } \mathbf{q} \leq \lambda \mathbf{w}_\eta(\tilde{\mathbf{x}}), \\ \infty & \text{otherwise,} \end{cases} \quad (27)$$

which implies that:

$$\text{prox}_{\sigma F_2^*}(\mathbf{q}) = \arg \min_{\mathbf{q}'} F_2^*(\mathbf{q}') + \frac{1}{2\sigma} \|\mathbf{q} - \mathbf{q}'\|_2^2 \quad (28)$$

$$= \frac{\lambda \mathbf{w}_\eta(\tilde{\mathbf{x}}) \odot \mathbf{q}}{\max(\lambda \mathbf{w}_\eta(\tilde{\mathbf{x}}), \mathbf{q})}, \quad (29)$$

where both the maximum and the division are taken element-wise. More details on the computation of the proximal operator of F_2^* can be found in [28].

Plugging these results into the CP scheme (20) with $\mathbf{z}^{(k)} = (\mathbf{p}^{(k)}, \mathbf{q}^{(k)})$ leads to the following updating rules:

$$\begin{cases} \mathbf{p}^{(k+1)} = \frac{\mathbf{p}^{(k)} + \sigma(\mathbf{K}\tilde{\mathbf{x}}^{(k)} - \mathbf{y}^\delta)}{1+3\sigma}, \\ \mathbf{q}^{(k+1)} = \frac{\lambda \mathbf{w}_\eta(\tilde{\mathbf{x}}) \odot (\mathbf{q}^{(k)} + \sigma |\mathbf{D}\tilde{\mathbf{x}}^{(k)}|)}{\max(\lambda \mathbf{w}_\eta(\tilde{\mathbf{x}}), \mathbf{q}^{(k)} + \sigma |\mathbf{D}\tilde{\mathbf{x}}^{(k)}|)}, \\ \mathbf{x}^{(k+1)} = \mathcal{P}_+ \left(\mathbf{x}^{(k)} - \tau \mathbf{M}^T \begin{bmatrix} \mathbf{p}^{(k+1)} \\ \mathbf{q}^{(k+1)} \end{bmatrix} \right), \\ \tilde{\mathbf{x}}^{(k+1)} = \mathbf{x}^{(k+1)} + \beta (\mathbf{x}^{(k+1)} - \mathbf{x}^{(k)}). \end{cases} \quad (30)$$

The corresponding CP algorithm is reported in Algorithm 1.

Algorithm 1 The Chambolle-Pock algorithm to solve Problem (2)

Require: a linear operator \mathbf{K} , corrupted data $\mathbf{y}^\delta \in \mathbb{R}^m$, a regularization parameter $\lambda > 0$, a reconstructor $\Psi : \mathbb{R}^m \rightarrow \mathbb{R}^n$

Require: $\tilde{\mathbf{x}}^0 = \mathbf{x}^0 \in \mathbb{R}^n$, $\mathbf{p}^{(0)} \in \mathbb{R}^m$, $\mathbf{q}^{(0)} \in \mathbb{R}^{2n}$

- 1: **define** $\mathbf{M} = [\mathbf{K}; \mathbf{D}]$, $\gamma \approx \|\mathbf{M}\|_2$, $\tau = \sigma = \gamma^{-1}$, $\beta = 1$, $\eta > 0$
 - 2: **initialize** $k = 0$
 - 3: **repeat**
 - 4: $\mathbf{p}^{(k+1)} = \frac{\mathbf{p}^{(k)} + \sigma(\mathbf{K}\tilde{\mathbf{x}}^{(k)} - \mathbf{y}^\delta)}{1+3\sigma}$ ▷ Update dual variables
 - 5: $\mathbf{q}^{(k+1)} = \frac{\lambda \mathbf{w}_\eta(\tilde{\mathbf{x}}) \odot (\mathbf{q}^{(k)} + \sigma |\mathbf{D}\tilde{\mathbf{x}}^{(k)}|)}{\max(\lambda \mathbf{w}_\eta(\tilde{\mathbf{x}}), \mathbf{q}^{(k)} + \sigma |\mathbf{D}\tilde{\mathbf{x}}^{(k)}|)}$
 - 6:
 - 7: $\mathbf{x}^{(k+1)} = \mathcal{P}_+ \left(\mathbf{x}^{(k)} - \tau \mathbf{M}^T \begin{bmatrix} \mathbf{p}^{(k+1)} \\ \mathbf{q}^{(k+1)} \end{bmatrix} \right)$ ▷ Update primal variable
 - 8:
 - 9: $\tilde{\mathbf{x}}^{(k+1)} = \mathbf{x}^{(k+1)} + \beta (\mathbf{x}^{(k+1)} - \mathbf{x}^{(k)})$ ▷ Update inertia term
 - 10:
 - 11: **update** $PDG(\mathbf{x}^{(k+1)}, \mathbf{p}^{(k+1)}, \mathbf{q}^{(k+1)})$ as in (31)
 - 12: **update** $k = k + 1$
 - 13: **until** $PDG(\mathbf{x}^{(k)}, \mathbf{p}^{(k)}, \mathbf{q}^{(k)}) \leq \epsilon_{\mathcal{J}}$ **or** $\|\mathbf{x}^{(k+1)} - \mathbf{x}^{(k)}\|_2 \leq \epsilon_{\mathbf{x}} \|\mathbf{x}^{(k)}\|_2$
-

We stop the CP iterations according to a combination of two convergence criteria: firstly, at any iteration, we check whether $\|\mathbf{x}^{(k+1)} - \mathbf{x}^{(k)}\|_2 \leq \epsilon_{\mathbf{x}} \|\mathbf{x}^{(k)}\|_2$, to stop the algorithm if the method get stucked on a flat region of the objective function. Secondly, as the Chambolle-Pock algorithm is a primal-dual method, we consider a primal-dual gap (PDG) criterium, terminating the iterations if:

$$\underbrace{F(\mathbf{M}\mathbf{x}^{(k)}) + G(\mathbf{x}^{(k)}) + G^* \left(\mathbf{M}^T \begin{bmatrix} \mathbf{p}^{(k)} \\ \mathbf{q}^{(k)} \end{bmatrix} \right) + F^* \left(\begin{bmatrix} \mathbf{p}^{(k)} \\ \mathbf{q}^{(k)} \end{bmatrix} \right)}_{\text{Primal-Dual Gap } PDG(\mathbf{x}^{(k)}, \mathbf{p}^{(k)}, \mathbf{q}^{(k)})} \leq \epsilon_{\mathcal{J}}. \quad (31)$$

We remark that the CP algorithm is convergent if both $F(\mathbf{M}\mathbf{x})$ and $G(\mathbf{x})$ are convex, proper and lower semi-continuous, with a theoretical convergence rate of $\mathcal{O}(\frac{1}{k^2})$ [8], and we fit these requirements.

4 Numerical experiments

In this Section, we present the numerical results obtained on some synthetic and real test images. The tests on synthetic images primarily aim to assess the potential of the model and analyze the method’s behavior in an optimal scenario. Real images, as such, inherently contain artifacts and some noise, which may not necessarily be desirable to reproduce in the reconstruction. On the other hand, they possess characteristics and areas of interest that cannot be perfectly replicated in a simulation.

In both cases we compute a test problem, by setting a very sparse fan beam geometry with 45 angles in the range $[0, 180]$ and computing a projection matrix \mathbf{K} by using Astra-Toolbox [30, 29] routines. The sinogram \mathbf{y}^δ is then computed from the ground truth image \mathbf{x}^{GT} , according to the image formation model in Equation (1). The noise \mathbf{e} is obtained by sampling $\mathbf{z} \sim \mathcal{N}(\mathbf{0}, \mathbf{I})$ and computing:

$$\mathbf{e} = \nu \frac{\mathbf{z}}{\|\mathbf{z}\|_2} \|\mathbf{y}\|_2,$$

where we indicated with \mathbf{y} the noiseless sinogram (i.e. with $\nu = 0$). Note that this formulation is equivalent to (1), with $\delta = \nu \|\mathbf{y}\|_2$.

We analyze the considered reconstructions by means of metrics such as the Relative Error (RE), the Peak Signal to Noise Ratio (PSNR) and the Structural Similarity Index (SSIM) defined in [31], with respect to the ground truth image.

To justify the choice of the space-variant parameter, we compare the results obtained from the proposed method with the global Total Variation regularization. In this case, the parameter λ has been chosen heuristically to minimize the relative error. Moreover, we conduct a comparative analysis of the outcomes achieved by varying the choice of the reconstructor Ψ , as discussed in Section 2.4. We also considered the case $\tilde{\mathbf{x}} = \mathbf{x}^{GT}$ for comparison. The methods are labeled as FBP- $W\ell_1$, TV- $W\ell_1$, NN- $W\ell_1$, and GT- $W\ell_1$. Notably, in the case of TV- $W\ell_1$ method, the CP method has been used to implement the Ψ reconstructor, prematurely terminated after 100 iterations. In the case of NN- $W\ell_1$, we have used $\alpha \in \{0, 0.5, 1\}$ in the elastic loss.

4.1 Experiments on a synthetic image

The synthetic image, depicted in Figure 3, contains objects of interest in tomography: homogeneous areas of regular shape simulating tumoral masses, high-density areas simulating bones or metal, and objects with very thin edges.

All considered methods were stopped at 10000 iterations, after ensuring that they satisfy the convergence criteria (31) with $\epsilon_{\mathcal{J}} = \epsilon_{\mathbf{x}} = 10^{-5}$. Since the image to be reconstructed has an extremely sparse gradient, the parameter η must be small and we have set $\eta = 2 \cdot 10^{-5}$ for all the methods.

We conducted two simulations: in the first instance, low noise was introduced with $\nu = 0.005$, while in the second case, ν was set to 0.02. For both simulations, Table 1 presents the metrics for both the $\tilde{\mathbf{x}}$ image and the reconstructed image $\mathbf{x}_{\Psi, \delta}^*$ across the various considered approaches.

We first consider the low noise projections obtained with $\nu = 0.005$; in this case we set $\lambda = 5$ for all the methods. Table 1 highlights that the reconstructions achieved through the proposed space-variant regularization method consistently demonstrate exceptional quality, as evidenced by SSIM values surpassing 0.99. Notably, this high quality persists despite considerable dissimilarity among the $\tilde{\mathbf{x}}$ images employed for computing the weights. Examination of RE and PSNR values reveals superior outcomes when utilizing, in sequential order, the GT- $W\ell_1$, the FBP- $W\ell_1$ and the TV- $W\ell_1$ approaches. Conversely, the global TV reconstruction yields the least favorable results across all metrics.

In Figure 3 we display the $\tilde{\mathbf{x}}$ images in the upper row and the corresponding weights $\mathbf{w}_\eta(\tilde{\mathbf{x}})$ in the lower row. The images computed by the FBP and TV reconstructors exhibit small noise but severe artifacts represented by streaks, which are due to the low number of views (45 out of 180 degrees). These artifacts are inherited by the $\mathbf{w}_\eta(\tilde{\mathbf{x}})$ weight images. The colorbar provides information about the range of the reconstructed values by the various methods. However, a quite large value of $\lambda = 5$ inhibits these defects and leads to a visually nearly perfect reconstruction (SSIM > 0.99).

In the subsequent test, we increased the noise ($\nu = 0.02$) and we set $\lambda = 10$ and $\eta = 2 \cdot 10^{-5}$ for all the methods except the case where Ψ is the FBP algorithm where $\eta = 2 \cdot 10^{-3}$. The results are reported in the lower part of Table 1 and the images are displayed in in Figure 4. The achieved results exhibit overall excellence in terms of SSIM (above all considering the sparsity of the tomographic data). However, as depicted in Figure 4, which showcases a crop of the restored images, discernible differences are evident in output, particularly in the reconstruction of the finer cross details and contrast. Notably, the global TV method consistently fails to reconstruct that cross regardless of the parameter value. The superior performance of the reconstruction when $\tilde{\mathbf{x}} = \mathbf{x}^{GT}$ underscores the efficacy of adapting regularization to image pixels when provided with a highly accurate approximation of the target image.

Table 1: Performance results on the synthetic image with low ($\nu = 0.005$) and medium ($\nu = 0.02$) noise. In the first three columns the metrics relative to the image \tilde{x} , in the last three columns the metrics relative to the output image $x_{\Psi,\delta}^*$.

		RE	\tilde{x} PSNR	SSIM	RE	x^* PSNR	SSIM
$\nu = 0.005$	GT- $W\ell_1$	0.0000	100.00	1.0000	0.0217	46.9881	0.9979
	FBP- $W\ell_1$	0.5056	19.6281	0.1974	0.0373	42.2662	0.9953
	TV- $W\ell_1$	0.2236	26.7167	0.7335	0.0621	37.8454	0.9920
	global TV	-	-	-	0.1236	31.8657	0.9805
$\nu = 0.02$	GT- $W\ell_1$	0.0000	100.00	1.0000	0.0398	41.7159	0.9968
	FBP- $W\ell_1$	0.9694	13.9748	0.0524	0.1025	33.4928	0.9809
	TV- $W\ell_1$	0.2435	25.9754	0.5968	0.0911	34.5162	0.9797
	global TV	-	-	-	0.1249	31.7715	0.9787

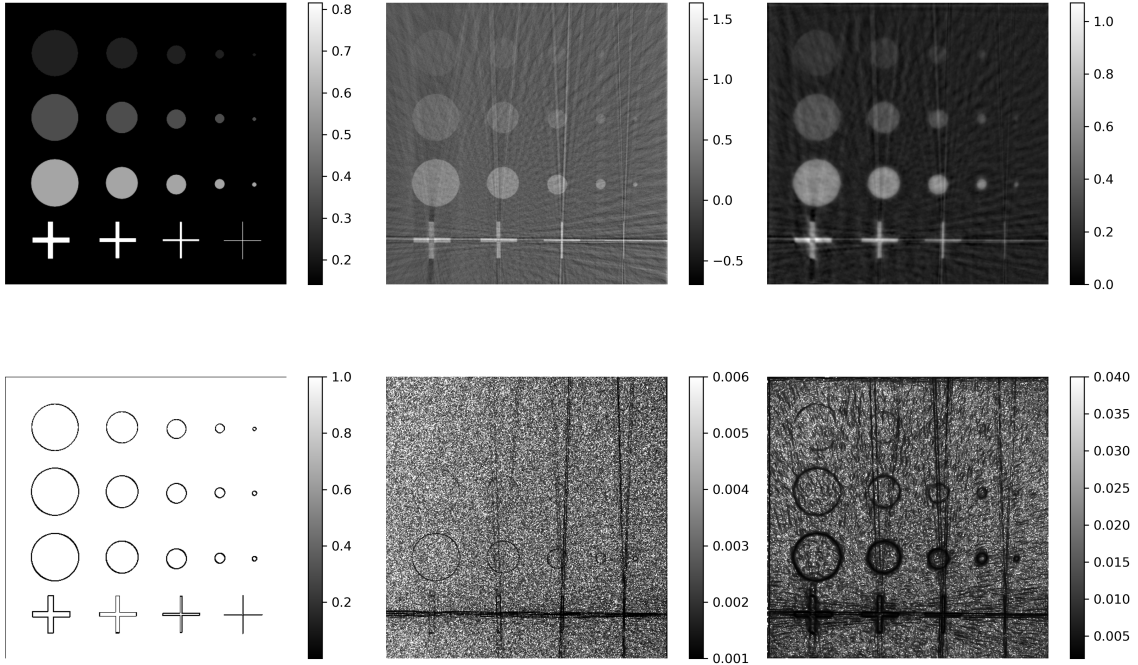


Figure 3: Experiment on the synthetic image with low noise ($\nu = 0.005$). In the first row, from left to right: \tilde{x}^{GT} , \tilde{x}^{FBP} , \tilde{x}^{TV} . In the second row: the corresponding images of weights $w_\eta(\tilde{x})$.

Figure 4 also includes plots illustrating the behavior of the objective function (on the left) and Relative Error (on the right) across iterations for the various examined approaches. It is noteworthy that, despite comparing distinct objective functions in the first plot, their trends exhibit similar descending patterns, ultimately converging to nearly identical values. In regards to the error plot, the order of the curves is maintained across all iterations, consistent with the sequence discussed in Table 2. The plots clearly indicate that the error ceases to decrease further, indicating that the best achievable reconstruction has been obtained for each method.

4.2 Experiments on real medical images

The second test image is a real chest tomographic image from Low Dose CT Grand Challenge data set by the Mayo Clinic, which is not part of the training set used for our neural network. The image is characterized by low-contrast regions and by high-contrast tiny details in the lungs. It is depicted with its crop in Figure 5. The aim of these

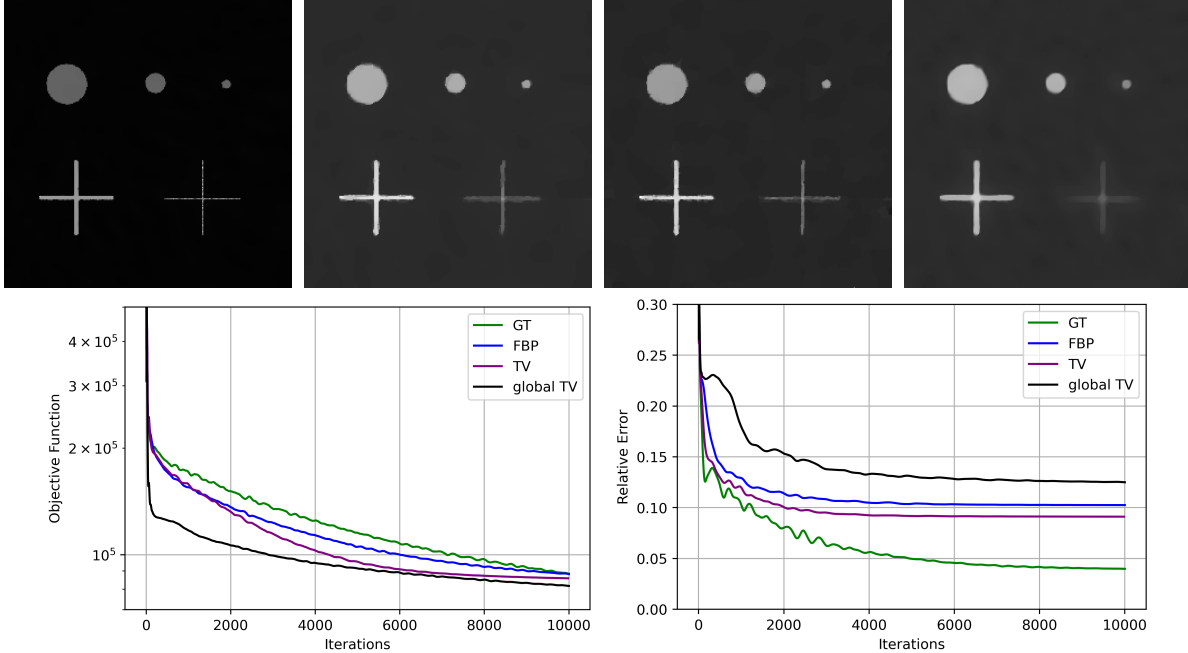


Figure 4: Results of the experiment on the synthetic image with high noise ($\nu = 0.02$). In the first row, from left to right: zooms on the lower-right angle of the reconstructions GT- $W\ell_1$, FBP- $W\ell_1$, TV- $W\ell_1$, global TV. In the second row: plot of the objective function (left) and of the Relative Error (right) over the iterations.

experiments is firstly to test the reconstructor Ψ_{Theta} constituted by the NN, and secondly to analyze the methods' performance on a real image with a gradient less sparse than in the synthetic, previous case.

We created the test problem as in the synthetic simulation and initially fixed $\nu = 0.005$. From the metrics reported in Table 2 we observe that the NN- $W\ell_1$ approach always overcomes the FBP- $W\ell_1$ in final quality. Regarding the elastic-loss of the neural network defined in (15), the best outcomes are attained with $\alpha = 1$, wherein the network learns merely gradients instead of the image. In fact, the \tilde{x} image is of low quality, yet the computed weights derived from it yield highly accurate reconstructions. Interestingly, setting $\alpha = 0.5$ gives the best \tilde{x} and the corresponding final solution has metrics very close to one achieved with $\alpha = 1$. In addition, in these two cases the behavior of the RE metric is highly comparable over the iterations, as visible in the plot in Figure 5.

In the final experiment, we introduce high noise by setting $\nu = 0.02$ and we apply the Ψ - $W\ell_1$ methods. In this case we start from the same image provided by the Ψ_{Θ} reconstructor (with $\alpha = 0.5$) and we consider various values for the parameter $\eta = 2 \cdot 10^{-3}, 2 \cdot 10^{-4}, 2 \cdot 10^{-5}$. Table 3 demonstrates that the value of η exerts a discrete influence on the quality of the output image, as also depicted in Figure 6. The initial column of the figure displays the masks in descending order of η from top to bottom. The second and third columns of Figure 6 correspond to the final reconstruction. The top image emphasizes the edges of the objects, the middle one smoothens the background to a value close to one, and the last one produces an excessively smooth image. Thus, the optimal reconstruction is attained with $\eta = 2 \cdot 10^{-4}$, representing the optimal compromise among the aforementioned reconstructions

Table 2: Performance results on the real image with low ($\nu = 0.005$) noise. In the first three columns the metrics relative to the image \tilde{x} , in the last three columns the metrics relative to the output image $x_{\Psi, \delta}^*$.

	\tilde{x}			$x_{\Psi, \delta}^*$		
	RE	PSNR	SSIM	RE	PSNR	SSIM
FBP- $W\ell_1$	0.2879	23.1629	0.4133	0.1009	32.2698	0.8832
NN- $W\ell_1$ ($\alpha = 0$)	0.1038	32.0253	0.8588	0.0893	33.3329	0.9009
NN- $W\ell_1$ ($\alpha = 0.5$)	0.0854	33.7229	0.8994	0.0836	33.9087	0.9121
NN- $W\ell_1$ ($\alpha = 1$)	0.5092	18.2113	0.3843	0.0834	33.9224	0.9128

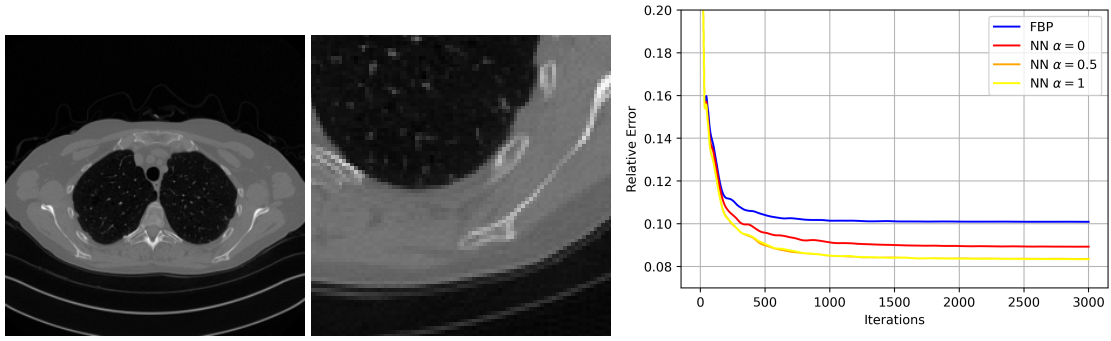


Figure 5: From left to right: ground truth image from Mayo data set, a cropped portion of it, a plot of the RE over iterations for the reconstructions by FBP- $W\ell_1$ and NN- $W\ell_1$ with $\alpha = 0, 0.5, 1$ ($\nu = 0.005$).

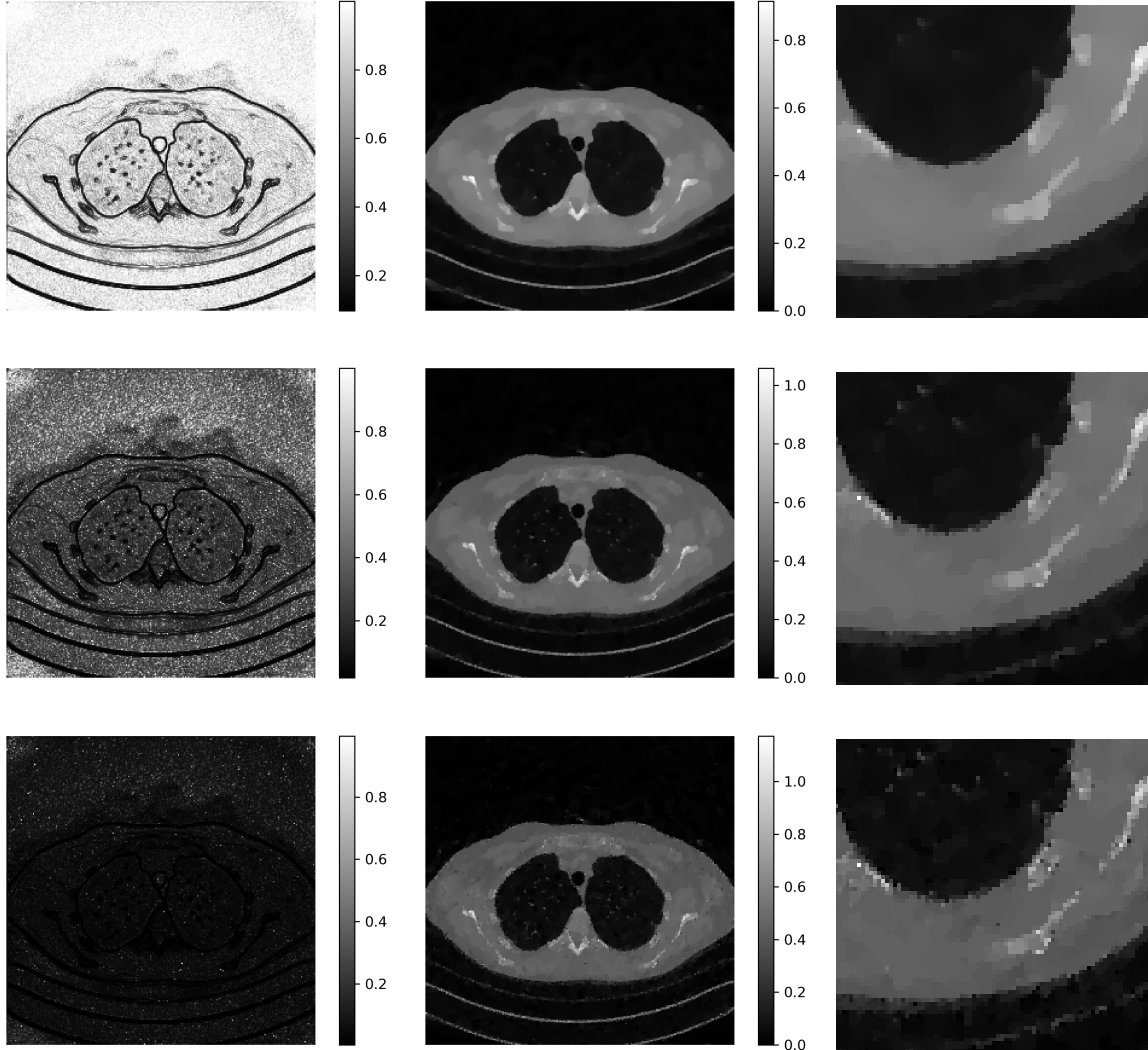


Figure 6: Results of the experiment on the real image with high noise ($\nu = 0.02$) with NN- $W\ell_1$. In the left column from top to down the images of the weights with $\eta = 2 \cdot 10^{-2}, \eta = 2 \cdot 10^{-3}, \eta = 2 \cdot 10^{-4}$; in the central column the corresponding reconstructions and in the right column a cropped portion of them.

Table 3: Performance results on the real image with high noise ($\nu = 0.02$). In the first three columns the metrics relative to the image \tilde{x} , in the last three columns the metrics relative to the output image $\mathbf{x}_{\Psi, \delta}^*$.

	\tilde{x}			$\mathbf{x}_{\Psi, \delta}^*$		
	RE	PSNR	SSIM	RE	PSNR	SSIM
FBP- $W\ell_1$	0.4910	18.5280	0.2118	0.1431	29.2351	0.8064
NN- $W\ell_1$ ($\eta = 2 \cdot 10^{-4}$)	0.1052	31.9065	0.8513	0.1473	28.9847	0.8078
NN- $W\ell_1$ ($\eta = 2 \cdot 10^{-3}$)	0.1052	31.9065	0.8513	0.1214	30.6619	0.8546
NN- $W\ell_1$ ($\eta = 2 \cdot 10^{-2}$)	0.1052	31.9065	0.8513	0.1219	30.6318	0.8421

5 Conclusion

In this paper, we propose a space-variant weighted Total Variation regularization method for reconstructing tomographic images from sparse views. Sparse-view CT constitutes an under-determined linear inverse problem, the solution of which is marked by noise and prominent artifacts. The proposed weighting strategies is obtained by linearizing a smoothed Total p-Variation, and by exploiting an image that we called \tilde{x} , without any prior knowledge of the noise characteristics in the data. We have used a data driven approach to effectively approximate the ground truth image or its gradients. Finally we have applied the space-variant Total Variation to a sinogram from very sparse geometry both of a synthetic and real image. The numerical results show that our model outperforms the global Total Variation, which uniformly acts on all the pixels of the image. Moreover, the best result is obtained when the information of the weights is retrieved from the ground truth, as demonstrated in the theoretical analysis. The approximation achieved by the neural network demonstrates its effectiveness, particularly when it learns to reconstruct the gradients of the images. The proposed spatially variant weighted approach can be easily extended to regularization methods other than Total Variation. In addition, we also intend to adaptively select the value of p in (14), in order to appropriately regularize both smooth and non-smooth regions of the image.

Declarations

5.1 Fundings

This work was partially supported by ‘‘Gruppo Nazionale per il Calcolo Scientifico (GNCS-INdAM)’’ (Progetto 2023 ‘‘Modelli e metodi avanzati in Computer Vision’’).

E. Loli Piccolomini, D. Evangelista and E. Morotti are supported by the PRIN 2022 project ‘‘STILE: Sustainable Tomographic Imaging with Learning and rEgularization’’, project code: 20225STXSB, funded by the European Commission under the NextGeneration EU programme.

A. Sebastiani is supported by the project ‘‘PNRR - Missione 4 ‘‘Istruzione e Ricerca’’ - Componente C2 Investimento 1.1 ‘‘Fondo per il Programma Nazionale di Ricerca e Progetti di Rilevante Interesse Nazionale (PRIN)’’, ‘‘Advanced optimization METHods for automated central veIn Sign detection in multiple sclerosis from magneTic resonAnce imaging (AMETISTA)’’, project code: P2022J9SNP, MUR D.D. financing decree n. 1379 of 1st September 2023 (CUP E53D23017980001) funded by the European Commission under the NextGeneration EU programme.

Conflict of interest. The authors declare that they have no conflict of interest in relation to the research presented in this paper.

Data availability. Under request to the authors.

Materials availability. Not applicable.

Code availability. Under request to the authors.

Appendix A Theoretical derivation of convergence results

In the following, we prove a stability result showing that $\|\mathbf{x}_{GT, \delta}^* - \mathbf{x}_{\Psi, \delta}^*\|_1$, i.e. the error introduced by using $\Psi(\mathbf{y}^\delta)$ instead of \mathbf{x}^{GT} into the computation of $\mathbf{w}_\eta(\tilde{x})$, converges to 0 as the distance $\|\Psi(\mathbf{y}^\delta) - \mathbf{x}^{GT}\|_1$ goes to 0.

We first need to introduce a preliminary result.

Proposition 11. Let $\{f_k\}_{k \in \mathbb{N}}$ be a sequence of functions converging uniformly to f^* on any compact subset of \mathcal{X} . Let us assume that for any $k \in \mathbb{N}$ it holds:

- (i) $\min_{\mathbf{x} \in \mathcal{X}} f_k(\mathbf{x})$ has a unique solution $\mathbf{x}_k \in \mathbb{R}^n$,
- (ii) $\min_{\mathbf{x} \in \mathcal{X}} f^*(\mathbf{x})$ has a unique solution $\mathbf{x}^* \in \mathbb{R}^n$.

Then:

$$\lim_{k \rightarrow \infty} \|\mathbf{x}_k - \mathbf{x}^*\|_1 = 0.$$

Proof. Let \mathbf{x}_k be the unique minimizer of f_k for any $k \in \mathbb{N}$ and let $C \subseteq \mathcal{X}$ be any compact set such that $\mathbf{x}_k \in C$ for any $k \in \mathbb{N}$. Since $\{\mathbf{x}_k\}_{k \in \mathbb{N}}$ is a sequence in a compact set, there exists a convergent subsequence $\{\mathbf{x}_{k_j}\}_{j \in \mathbb{N}}$. Let \mathbf{x}^* be the limit of this subsequence. By definition, for any $k \in \mathbb{N}$, it holds:

$$f_k(\mathbf{x}_k) \leq f_k(\mathbf{x}), \quad \forall \mathbf{x} \in C,$$

and in particular:

$$f_{k_j}(\mathbf{x}_{k_j}) \leq f_{k_j}(\mathbf{x}), \quad \forall \mathbf{x} \in C.$$

Since f_k converges uniformly to f^* and \mathbf{x}_{k_j} converges to \mathbf{x}^* , it holds that:

$$\begin{aligned} \lim_{j \rightarrow \infty} f_{k_j}(\mathbf{x}_{k_j}) &= f^*(\mathbf{x}^*), \\ \lim_{j \rightarrow \infty} f_{k_j}(\mathbf{x}) &= f^*(\mathbf{x}), \quad \forall \mathbf{x} \in C. \end{aligned}$$

Consequently,

$$f^*(\mathbf{x}^*) \leq f^*(\mathbf{x}), \quad \forall \mathbf{x} \in C,$$

i.e. \mathbf{x}^* is a minimizer of f^* . Since f^* has a unique minimizer, then all the subsequences of \mathbf{x}_k converge to the same element \mathbf{x}^* , which implies that \mathbf{x}_k converges to \mathbf{x}^* as $k \rightarrow \infty$. In particular:

$$\lim_{k \rightarrow \infty} \|\mathbf{x}_k - \mathbf{x}^*\|_1 = 0.$$

□

Now, revisiting the definition of the Ψ reconstructor introduced in Section 2.3, we expound upon the notions of p -norm accuracy η_p^{-1} and p -norm ϵ -stability constant $C_{\Psi, p}^\epsilon$ associated with Ψ , thereby extending the concepts initially introduced in [15, 14].

Definition 1. Let $\Psi : \mathbb{R}^m \rightarrow \mathbb{R}^n$ be a reconstructor. Let:

$$\eta_p := \sup_{\mathbf{x} \in \mathcal{X}} \|\Psi(\mathbf{K}\mathbf{x}) - \mathbf{x}\|_p.$$

If $\eta_p < \infty$, we say the Ψ is η_p^{-1} -accurate in p -norm.

Definition 2. Let $\Psi : \mathbb{R}^m \rightarrow \mathbb{R}^n$ be an η_p^{-1} -accurate reconstructor in p -norm. Then, for any $\epsilon > 0$, we say that $C_{\Psi, p}^\epsilon$ is the p -norm ϵ -stability constant if:

$$C_{\Psi, p}^\epsilon = \sup_{\substack{\mathbf{x} \in \mathcal{X} \\ \|\mathbf{e}\|_p \leq \epsilon}} \frac{\|\Psi(\mathbf{K}\mathbf{x} + \mathbf{e}) - \mathbf{x}\|_p - \eta_p}{\|\mathbf{e}\|_p}.$$

For an analysis of the accuracy and the stability constant of a reconstructor, see [15] where the case $p = 2$ is explored in detail. Note that most of the results obtained for $p = 2$ can be easily extended to $p \geq 1$. In the context of this study, we emphasize that η_p delineates the upper bound on the reconstruction error (measured in the p -norm) incurred by the reconstructor Ψ when applied to noiseless data (when $\delta = 0$). Conversely, $C_{\Psi, p}^\epsilon$ serves as a metric quantifying the amplification (or reduction), provided by Ψ , of input noise, which is upper bounded within a p -norm by ϵ in the data, since Definition 2 can be rewritten as:

$$\|\Psi(\mathbf{K}\mathbf{x} + \mathbf{e}) - \mathbf{x}\|_p \leq \eta_p + C_{\Psi, p}^\epsilon \|\mathbf{e}\|_p, \quad \forall \|\mathbf{e}\|_p \leq \epsilon, \mathbf{x} \in \mathcal{X}. \quad (32)$$

Now, we need to prove a couple of results.

Proposition 12. For any $\delta > 0$ and any $\eta > 0$, $w_\eta(\tilde{\mathbf{x}})$ defined in Equation (13) is a Lipschitz continuous function of $|\mathbf{D}\tilde{\mathbf{x}}|$ in 1-norm, i.e. there exists $L(w_\eta) \geq 0$, such that for any $\tilde{\mathbf{x}}, \tilde{\mathbf{x}}' \in \mathcal{X}$:

$$\|w_\eta(\tilde{\mathbf{x}}) - w_\eta(\tilde{\mathbf{x}}')\|_1 \leq L(w_\eta) \left| |\mathbf{D}\tilde{\mathbf{x}}| - |\mathbf{D}\tilde{\mathbf{x}}'| \right|_1.$$

Proof. If we consider:

$$f(\alpha) = \left(\frac{\eta}{\sqrt{\eta^2 + \alpha^2}} \right)^{1-p},$$

the proof trivially follows from the observation that $f'(\alpha)$ is a continuous function of α . Indeed:

$$f'(\alpha) = (p-1) \frac{\alpha}{\sqrt{\eta^2 + \alpha^2}} \left(\frac{\eta}{\sqrt{\eta^2 + \alpha^2}} \right)^{p-2},$$

which is continuous everywhere if $\eta \neq 0$. □

From now on, we denote as:

$$\mathcal{J}_{GT}(\mathbf{x}, \mathbf{y}^\delta) := \frac{1}{2} \|\mathbf{K}\mathbf{x} - \mathbf{y}^\delta\|_2^2 + \lambda \|w_\eta(\mathbf{x}^{GT}) \odot |\mathbf{D}\mathbf{x}|\|_1. \quad (33)$$

the objective function of our regularized model, where the ground truth image \mathbf{x}^{GT} is used in place of $\tilde{\mathbf{x}}$ in the weighted strategy. We can thus prove the following inequality.

Proposition 13. For any $\mathbf{x} \in \mathcal{X}$, any fixed $\delta > 0$ and any $\mathbf{y}^\delta \in \mathbb{R}^m$, it holds:

$$|\mathcal{J}_{GT}(\mathbf{x}, \mathbf{y}^\delta) - \mathcal{J}(\mathbf{x}, \mathbf{y}^\delta)| \leq \lambda L(w_\eta) \|\mathbf{D}\|_{2,1} (\eta_1 + C_{\Psi,1}^\epsilon \|e\|_1) \|\mathbf{D}\mathbf{x}\|_{2,1}, \quad (34)$$

where η_1 and $C_{\Psi,1}^\epsilon$ are the accuracy and the ϵ -stability constant in 1-norm of Ψ , respectively, $\epsilon > 0$ is the maximum norm of the noise e in \mathbf{y}^δ , and \mathcal{J}_{GT} is given by Equation (33).

Proof. We first note that:

$$\mathcal{J}_{GT}(\mathbf{x}, \mathbf{y}^\delta) - \mathcal{J}(\mathbf{x}, \mathbf{y}^\delta) = \lambda (\|w_\eta(\mathbf{x}^{GT}) \odot |\mathbf{D}\mathbf{x}|\|_1 - \|w_\eta(\Psi(\mathbf{y}^\delta)) \odot |\mathbf{D}\mathbf{x}|\|_1).$$

Thus,

$$\begin{aligned} |\mathcal{J}_{GT}(\mathbf{x}, \mathbf{y}^\delta) - \mathcal{J}(\mathbf{x}, \mathbf{y}^\delta)| &= \lambda \left| \|w_\eta(\mathbf{x}^{GT}) \odot |\mathbf{D}\mathbf{x}|\|_1 - \|w_\eta(\Psi(\mathbf{y}^\delta)) \odot |\mathbf{D}\mathbf{x}|\|_1 \right| \\ &\leq \lambda \left| \|w_\eta(\mathbf{x}^{GT}) \odot |\mathbf{D}\mathbf{x}|\|_1 - \|w_\eta(\Psi(\mathbf{y}^\delta)) \odot |\mathbf{D}\mathbf{x}|\|_1 \right| \end{aligned}$$

by the reverse triangular inequality.

Now, let $\mathbf{W}_\eta(\tilde{\mathbf{x}})$ be the $n \times n$ diagonal matrix, whose diagonal entries are the elements of $w_\eta(\tilde{\mathbf{x}})$, so that $w_\eta(\tilde{\mathbf{x}}) \odot |\mathbf{D}\mathbf{x}| = \mathbf{W}_\eta(\tilde{\mathbf{x}}) |\mathbf{D}\mathbf{x}|$. Consequently, it holds:

$$\begin{aligned} |\mathcal{J}_{GT}(\mathbf{x}, \mathbf{y}^\delta) - \mathcal{J}(\mathbf{x}, \mathbf{y}^\delta)| &\leq \lambda \left\| \mathbf{W}_\eta(\mathbf{x}^{GT}) |\mathbf{D}\mathbf{x}| - \mathbf{W}_\eta(\Psi(\mathbf{y}^\delta)) |\mathbf{D}\mathbf{x}| \right\|_1 \\ &= \lambda \left\| (\mathbf{W}_\eta(\mathbf{x}^{GT}) - \mathbf{W}_\eta(\Psi(\mathbf{y}^\delta))) |\mathbf{D}\mathbf{x}| \right\|_1 \\ &\leq \lambda \left\| \mathbf{W}_\eta(\mathbf{x}^{GT}) - \mathbf{W}_\eta(\Psi(\mathbf{y}^\delta)) \right\|_1 \|\mathbf{D}\mathbf{x}\|_1. \end{aligned}$$

From Proposition 12, it follows:

$$\left\| \mathbf{W}_\eta(\mathbf{x}^{GT}) - \mathbf{W}_\eta(\Psi(\mathbf{y}^\delta)) \right\|_1 \leq L(w_\eta) \left| |\mathbf{D}\mathbf{x}^{GT}| - |\mathbf{D}\Psi(\mathbf{y}^\delta)| \right|_1,$$

where $L(w_\eta)$ is the Lipschitz constant of w_η .

To go on, note that the reverse triangular inequality gives:

$$\left| \|\mathbf{D}\mathbf{x}^{GT}\|_1 - \|\mathbf{D}\Psi(\mathbf{y}^\delta)\|_1 \right| \leq \left\| \mathbf{D}\mathbf{x}^{GT} - \mathbf{D}\Psi(\mathbf{y}^\delta) \right\|_1 = \left\| \mathbf{D}(\mathbf{x}^{GT} - \Psi(\mathbf{y}^\delta)) \right\|_{2,1},$$

where $\|\cdot\|_{2,1}$ is defined in (6). Now, let $\|\mathbf{D}\|_{2,1}$ be the matrix norm induced by the $\|\cdot\|_{2,1}$ vector norm, i.e.:

$$\|\mathbf{D}\|_{2,1} := \max_{\mathbf{x} \in \mathbb{R}^n} \frac{\|\mathbf{D}\mathbf{x}\|_{2,1}}{\|\mathbf{x}\|_1}.$$

We get:

$$\|\mathbf{D}(\mathbf{x}^{GT} - \Psi(\mathbf{y}^\delta))\|_{2,1} \leq \|\mathbf{D}\|_{2,1} \|\mathbf{x}^{GT} - \Psi(\mathbf{y}^\delta)\|_1.$$

To conclude, let $\epsilon > 0$ be the maximum norm of \mathbf{e} in $\mathbf{y}^\delta = \mathbf{K}\mathbf{x}^{GT} + \mathbf{e}$. By Equation (32), following from Definition 2:

$$\|\mathbf{x}^{GT} - \Psi(\mathbf{y}^\delta)\|_1 = \|\mathbf{x}^{GT} - \Psi(\mathbf{K}\mathbf{x}^{GT} + \mathbf{e})\|_1 \leq \eta_1 + C_{\Psi,1}^\epsilon \|\mathbf{e}\|_1,$$

where η_1 and $C_{\Psi,1}^\epsilon$ are the accuracy and the ϵ -stability constant in 1-norm of Ψ , respectively. In conclusion, we have obtained the following inequality:

$$|\mathcal{J}_{GT}(\mathbf{x}, \mathbf{y}^\delta) - \mathcal{J}(\mathbf{x}, \mathbf{y}^\delta)| \leq \lambda L(\mathbf{w}_\eta) \|\mathbf{D}\|_{2,1} (\eta_1 + C_{\Psi,1}^\epsilon \|\mathbf{e}\|_1) \|\mathbf{D}\mathbf{x}\|_1,$$

which proves the result. □

To proceed, we first consider the noiseless case (i.e. $\delta = 0$), for which it holds the following Proposition.

Proposition 14. *Let $\mathbf{x}_{GT,0}^*$ be the unique minimum of $\mathcal{J}_{GT}(\mathbf{x}, \mathbf{y}^\delta)$, defined in (33), with $\delta = 0$. Let $\{\Psi_k\}_{k \in \mathbb{N}}$ be a sequence of reconstructors, each with accuracy $\eta_{1,k}^{-1}$ in 1-norm. Let $\mathbf{x}_{k,0}^*$ be the unique minimum of $\mathcal{J}_k(\mathbf{x}, \mathbf{y}^0) := \mathcal{J}(\mathbf{x}, \mathbf{y}^0)$ with $\Psi = \Psi_k$ and $\delta = 0$. Then, if $\eta_{1,k} \rightarrow 0$ for $k \rightarrow \infty$:*

$$\|\mathbf{x}_{GT,0}^* - \mathbf{x}_{k,0}^*\|_1 \rightarrow 0.$$

Proof. If $\delta = 0$, then for any $k \in \mathbb{N}$, Proposition 13 implies:

$$\begin{aligned} |\mathcal{J}_{GT}(\mathbf{x}, \mathbf{y}^0) - \mathcal{J}_k(\mathbf{x}, \mathbf{y}^0)| &\leq \eta_{1,k} L(\mathbf{w}_\eta) \|\mathbf{D}\|_{2,1} \|\mathbf{D}\mathbf{x}\|_{2,1} \leq \eta_{1,k} L(\mathbf{w}_\eta) \|\mathbf{D}\|_{2,1}^2 \|\mathbf{x}\|_1 \\ &\leq \eta_{1,k} n L(\mathbf{w}_\eta) \|\mathbf{D}\|_{2,1}^2 \|\mathbf{x}\|_\infty, \end{aligned}$$

which, considering that $\eta_{1,k} \rightarrow 0$ as $k \rightarrow \infty$, implies that $\mathcal{J}_k(\mathbf{x}, \mathbf{y}^0) \rightarrow \mathcal{J}_{GT}(\mathbf{x}, \mathbf{y}^0)$ uniformly on every compact subset of \mathcal{X} .

Let $C \subseteq \mathcal{X}$ be the closure of any set that contains $\mathbf{x}_{k,0}^*$ for all $k \in \mathbb{N}$. C is limited, indeed let $\mathbf{x}^\dagger \in \mathbb{R}^n$ be a solution of $\mathbf{K}\mathbf{x} = \mathbf{y}^0$, then for any $k \in \mathbb{N}$:

$$\lambda \|\mathbf{w}_\eta(\Psi_k(\mathbf{y}^0)) \odot |\mathbf{D}\mathbf{x}_{k,0}^*|\|_1 \leq \mathcal{J}_k(\mathbf{x}_{k,0}^*, \mathbf{y}^0) \leq \mathcal{J}_k(\mathbf{x}^\dagger, \mathbf{y}^0) = \lambda \|\mathbf{w}_\eta(\Psi_k(\mathbf{y}^0)) \odot |\mathbf{D}\mathbf{x}^\dagger|\|_1,$$

where the second inequality comes from the definition of minimizer. By Proposition 8 $\mathbf{w}_\eta(\Psi_k(\mathbf{y}^0)) \leq \mathbf{1}$, thus:

$$\lambda \|\mathbf{w}_\eta(\Psi_k(\mathbf{y}^0)) \odot |\mathbf{D}\mathbf{x}_{k,0}^*|\|_1 \leq \lambda \|\mathbf{w}_\eta(\Psi_k(\mathbf{y}^0)) \odot |\mathbf{D}\mathbf{x}^\dagger|\|_1 \leq \lambda \|\mathbf{D}\mathbf{x}^\dagger\|_{2,1} = c < \infty.$$

Consequently,

$$\lim_{k \rightarrow \infty} \lambda \|\mathbf{w}_\eta(\Psi_k(\mathbf{y}^0)) \odot |\mathbf{D}\mathbf{x}_{k,0}^*|\|_1 < \infty,$$

which, since $\lambda \|\mathbf{w}_\eta(\Psi_k(\mathbf{y}^0)) \odot |\mathbf{D}\mathbf{x}_{k,0}^*|\|_1$ is coercive, implies that $\{\mathbf{x}_k\}_{k \in \mathbb{N}}$ is limited, and so is C .

Since C is closed and limited, it is compact, and thus $\mathcal{J}_k(\mathbf{x}, \mathbf{y}^0) \rightarrow \mathcal{J}_{GT}(\mathbf{x}, \mathbf{y}^0)$ uniformly in C . Since $\mathbf{x}_{k,0}^*$ is unique by Theorem 6, by Proposition 11, $\|\mathbf{x}_{k,0}^* - \mathbf{x}_{GT,0}^*\|_1 \rightarrow 0$ as $k \rightarrow \infty$. □

We can also prove a convergence result for $\mathbf{x}_{GT,\delta}^*$ and $\mathbf{x}_{\Psi,\delta}^*$.

Proposition 15. *Let $\{\delta_k\}_{k \in \mathbb{N}}$ be any sequence of positive noise levels such that $\delta_k \rightarrow 0$ as $k \rightarrow \infty$. For any $k \in \mathbb{N}$, let $\mathbf{x}_{GT,\delta_k}^*$ be the unique minimizer of $\mathcal{J}_{GT}(\mathbf{x}, \mathbf{y}^{\delta_k})$. Then:*

$$\lim_{k \rightarrow \infty} \|\mathbf{x}_{GT,\delta_k}^* - \mathbf{x}_{GT,0}^*\|_1 \rightarrow 0.$$

Proof. Note that $\mathcal{J}_{GT}(\mathbf{x}, \mathbf{y}^{\delta_k})$ is continuous with respect to \mathbf{y}^{δ_k} , since the term \mathbf{y}^{δ_k} appears in $\mathcal{J}_{GT}(\mathbf{x}, \mathbf{y}^{\delta_k})$ only via a quadratic term. Consequently,

$$\lim_{k \rightarrow \infty} \mathcal{J}_{GT}(\mathbf{x}, \mathbf{y}^{\delta_k}) = \mathcal{J}_{GT}(\mathbf{x}, \mathbf{y}^0), \quad \forall \mathbf{x} \in \mathcal{X}. \quad (35)$$

To prove the result, we need to show that $\mathcal{J}_{GT}(\mathbf{x}, \mathbf{y}^{\delta_k})$ converges uniformly to $\mathcal{J}_{GT}(\mathbf{x}, \mathbf{y}^0)$ in \mathbf{x} on any compact, which together with the uniqueness of the minimizer, implies that $\mathbf{x}_{GT, \delta_k}^*$ converges to $\mathbf{x}_{GT, 0}^*$ as $k \rightarrow \infty$ by Proposition 11. To this aim, we observe that for any $\mathbf{x} \in \mathcal{X}$:

$$\begin{aligned} |\mathcal{J}_{GT}(\mathbf{x}, \mathbf{y}^{\delta_k}) - \mathcal{J}_{GT}(\mathbf{x}, \mathbf{y}^0)| &= \left| \frac{1}{2} \|\mathbf{K}\mathbf{x} - \mathbf{y}^{\delta_k}\|_2^2 - \frac{1}{2} \|\mathbf{K}\mathbf{x} - \mathbf{y}^0\|_2^2 \right| \\ &\leq \frac{1}{2} \|\mathbf{K}\mathbf{x} - \mathbf{y}^{\delta_k} - (\mathbf{K}\mathbf{x} - \mathbf{y}^0)\|_2^2 \\ &= \frac{1}{2} \|\mathbf{y}^{\delta_k} - \mathbf{y}^0\|_2^2 \leq \frac{1}{2} \delta_k^2. \end{aligned}$$

Since δ_k does not depend on \mathbf{x} , and $\delta_k \rightarrow 0$ as $k \rightarrow \infty$, then this implies that $\mathcal{J}_{GT}(\mathbf{x}, \mathbf{y}^{\delta_k})$ converges to $\mathcal{J}_{GT}(\mathbf{x}, \mathbf{y}^0)$ uniformly. This proves that $\mathbf{x}_{GT, \delta_k}^*$ converges to $\mathbf{x}_{GT, 0}^*$ and, in particular,

$$\lim_{k \rightarrow \infty} \|\mathbf{x}_{GT, \delta_k}^* - \mathbf{x}_{GT, 0}^*\|_1 = 0.$$

□

The convergence of $\mathbf{x}_{\Psi, \delta}^*$ to $\mathbf{x}_{\Psi, 0}^*$ as $\delta \rightarrow 0$ for a general reconstructor Ψ is slightly harder, since in this case, the regularizer also depends on δ due to $\tilde{\mathbf{x}} = \Psi(\mathbf{y}^\delta)$.

Proposition 16. *For any reconstructor $\Psi : \mathbb{R}^m \rightarrow \mathbb{R}^n$, let $\{\delta_k\}_{k \in \mathbb{N}}$ be any sequence of positive noise levels such that $\delta_k \rightarrow 0$ as $k \rightarrow \infty$. For any $k \in \mathbb{N}$, let $\mathbf{x}_{\Psi, \delta_k}^*$ be the unique minimizer of $\mathcal{J}(\mathbf{x}, \mathbf{y}^{\delta_k})$. Then:*

$$\lim_{k \rightarrow \infty} \|\mathbf{x}_{\Psi, \delta_k}^* - \mathbf{x}_{\Psi, 0}^*\|_1 \rightarrow 0.$$

Proof. We proceed as in the proof of Proposition 15, denoting by $\mathcal{R}_k(\mathbf{x})$ the value of the regularizer with weights computed by $\Psi(\mathbf{y}^{\delta_k})$ for the sake of simplicity, namely i.e. $\mathcal{R}_k(\mathbf{x}) = \|\mathbf{w}_\eta(\Psi(\mathbf{y}^{\delta_k})) \odot \mathbf{D}\mathbf{x}\|_1$.

$$\begin{aligned} |\mathcal{J}(\mathbf{x}, \mathbf{y}^{\delta_k}) - \mathcal{J}(\mathbf{x}, \mathbf{y}^0)| &= \left| \frac{1}{2} \|\mathbf{K}\mathbf{x} - \mathbf{y}^{\delta_k}\|_2^2 - \frac{1}{2} \|\mathbf{K}\mathbf{x} - \mathbf{y}^0\|_2^2 + \lambda (\mathcal{R}_k(\mathbf{x}) - \mathcal{R}_0(\mathbf{x})) \right| \\ &\leq \left| \frac{1}{2} \|\mathbf{K}\mathbf{x} - \mathbf{y}^{\delta_k}\|_2^2 - \frac{1}{2} \|\mathbf{K}\mathbf{x} - \mathbf{y}^0\|_2^2 \right| + \lambda |\mathcal{R}_k(\mathbf{x}) - \mathcal{R}_0(\mathbf{x})| \\ &\leq \frac{1}{2} \delta_k^2 + \lambda |\mathcal{R}_k(\mathbf{x}) - \mathcal{R}_0(\mathbf{x})|, \end{aligned}$$

The second term can be rearranged by means of Proposition 12,

$$\begin{aligned} |\mathcal{R}_k(\mathbf{x}) - \mathcal{R}_0(\mathbf{x})| &= \left| \|\mathbf{w}_\eta(\Psi(\mathbf{y}^{\delta_k})) \odot \mathbf{D}\mathbf{x}\|_1 - \|\mathbf{w}_\eta(\Psi(\mathbf{y}^0)) \odot \mathbf{D}\mathbf{x}\|_1 \right| \\ &\leq \|\mathbf{w}_\eta(\Psi(\mathbf{y}^{\delta_k})) \odot \mathbf{D}\mathbf{x} - \mathbf{w}_\eta(\Psi(\mathbf{y}^0)) \odot \mathbf{D}\mathbf{x}\|_1 \\ &= \|(\mathbf{w}_\eta(\Psi(\mathbf{y}^{\delta_k})) - \mathbf{w}_\eta(\Psi(\mathbf{y}^0))) \odot \mathbf{D}\mathbf{x}\|_1 \\ &\leq \|\mathbf{w}_\eta(\Psi(\mathbf{y}^{\delta_k})) - \mathbf{w}_\eta(\Psi(\mathbf{y}^0))\|_1 \|\mathbf{D}\mathbf{x}\|_{2,1} \\ &\leq \|\mathbf{w}_\eta(\Psi(\mathbf{y}^{\delta_k})) - \mathbf{w}_\eta(\Psi(\mathbf{y}^0))\|_1 \|\mathbf{D}\|_{2,1} \|\mathbf{x}\|_1 \\ &\leq \|\mathbf{w}_\eta(\Psi(\mathbf{y}^{\delta_k})) - \mathbf{w}_\eta(\Psi(\mathbf{y}^0))\|_1 \|\mathbf{D}\|_{2,1} n \|\mathbf{x}\|_\infty \\ &\leq L(\mathbf{w}_\eta) \|\Psi(\mathbf{y}^{\delta_k}) - \Psi(\mathbf{y}^0)\|_1 \|\mathbf{D}\|_{2,1} n \|\mathbf{x}\|_\infty \\ &\leq L(\mathbf{w}_\eta) L(\Psi) \delta_k \|\mathbf{D}\|_{2,1} n \|\mathbf{x}\|_\infty, \end{aligned}$$

where $L(\Psi)$ is the Lipschitz constant of Ψ , which is well defined since Ψ is Lipschitz continuous by definition.

To summarize, we proved that:

$$|\mathcal{J}(\mathbf{x}, \mathbf{y}^{\delta_k}) - \mathcal{J}(\mathbf{x}, \mathbf{y}^0)| \leq \frac{1}{2} \delta_k^2 + \lambda L(\mathbf{w}_\eta) L(\Psi) \delta_k \|\mathbf{D}\|_{2,1} n \|\mathbf{x}\|_\infty,$$

which implies that $\mathcal{J}(\mathbf{x}, \mathbf{y}^{\delta_k})$ converges uniformly to $\mathcal{J}(\mathbf{x}, \mathbf{y}^0)$ on any compact subset of \mathcal{X} . By considering the closed subset C of \mathcal{X} that contains the sequence $\{\mathbf{x}_{\Psi, \delta_k}^*\}_{k \in \mathbb{N}}$, we conclude as in Proposition 15, by observing that C

is limited since:

$$\begin{aligned}
 \|\mathbf{w}_\eta(\Psi(\mathbf{y}^{\delta_k})) \odot |\mathbf{D}\mathbf{x}_{\Psi, \delta_k}^*|\|_1 &\leq \mathcal{J}_\Psi(\mathbf{x}_{\Psi, \delta_k}^*, \mathbf{y}^{\delta_k}) \leq \mathcal{J}_\Psi(\mathbf{x}^\dagger, \mathbf{y}^{\delta_k}) \\
 &\leq \frac{\delta_k^2}{2} + \lambda \|\mathbf{w}_\eta(\Psi(\mathbf{y}^{\delta_k})) \odot |\mathbf{D}\mathbf{x}^\dagger|\|_1 \\
 &\leq \frac{\delta_k^2}{2} + \lambda \|\mathbf{D}\mathbf{x}^\dagger\|_{2,1} \rightarrow c < \infty,
 \end{aligned}$$

where \mathbf{x}^\dagger is any solution of $\mathbf{K}\mathbf{x} = \mathbf{y}^0$, and $\|\mathbf{w}_\eta(\Psi(\mathbf{y}^{\delta_k})) \odot |\mathbf{D}\mathbf{x}_{\Psi, \delta_k}^*|\|_1$ is coercive. □

In conclusion, we observe that the stability results from Proposition 14 can be generalized to the case where $\delta > 0$. Thus, we can now prove Theorem 9.

Proof. Let:

$$\mathcal{J}_k(\mathbf{x}, \mathbf{y}^\delta) := \frac{1}{2} \|\mathbf{K}\mathbf{x} - \mathbf{y}^\delta\|_2^2 + \lambda \|\mathbf{w}_\eta(\Psi_k(\mathbf{y}^\delta)) \odot |\mathbf{D}\mathbf{x}|\|_1.$$

By proceeding as in the proof of Proposition 13, we can show that:

$$|\mathcal{J}_k(\mathbf{x}, \mathbf{y}^\delta) - \mathcal{J}_{GT}(\mathbf{x}, \mathbf{y}^\delta)| \leq \lambda L(\mathbf{w}_\eta) \left(\|\mathbf{D}\mathbf{x}^{GT}\|_1 - \|\mathbf{D}\Psi_k(\mathbf{y}^\delta)\|_1 \right) \|\mathbf{D}\mathbf{x}\|_{2,1},$$

where $L(\mathbf{w}_\eta)$ is defined as in Proposition 12. Consequently:

$$|\mathcal{J}_k(\mathbf{x}, \mathbf{y}^\delta) - \mathcal{J}_{GT}(\mathbf{x}, \mathbf{y}^\delta)| \leq n\lambda L(\mathbf{w}_\eta) \|\mathbf{D}\|_{2,1} \|\mathbf{x}\|_\infty \left(\|\mathbf{D}\mathbf{x}^{GT}\|_1 - \|\mathbf{D}\Psi_k(\mathbf{y}^\delta)\|_1 \right),$$

which implies that $\mathcal{J}_k(\mathbf{x}, \mathbf{y}^\delta)$ converges to $\mathcal{J}_{GT}(\mathbf{x}, \mathbf{y}^\delta)$ uniformly on any compact set, whenever

$$\lim_{k \rightarrow \infty} \left(\|\mathbf{D}\mathbf{x}^{GT}\|_1 - \|\mathbf{D}\Psi_k(\mathbf{y}^\delta)\|_1 \right) = 0.$$

By Proposition 11, we conclude that:

$$\lim_{k \rightarrow \infty} \|\mathbf{x}_{GT, \delta}^* - \mathbf{x}_{\Psi_k, \delta}^*\|_1 = 0.$$

□

References

- [1] Heinz H Bauschke, Patrick L Combettes, Heinz H Bauschke, and Patrick L Combettes. *Convex Analysis and Monotone Operator Theory in Hilbert Spaces*. Springer, 2017.
- [2] A Benfenati, P Causin, MG Lupieri, and G Naldi. Regularization techniques for inverse problem in dot applications. *Journal of Physics: Conference Series*, 1476(1):012007, mar 2020.
- [3] Villiam Bortolotti, RJS Brown, P Fantazzini, Germana Landi, and Fabiana Zama. Uniform penalty inversion of two-dimensional nmr relaxation data. *Inverse Problems*, 33(1):015003, 2016.
- [4] Tatiana A Bubba, Gitta Kutyniok, Matti Lassas, Maximilian März, Wojciech Samek, Samuli Siltanen, and Vignesh Srinivasan. Learning the invisible: A hybrid deep learning-shearlet framework for limited angle computed tomography. *Inverse Problems*, 35(6):064002, 2019.
- [5] Emmanuel J Candès, Michael B Wakin, and Stephen P Boyd. Enhancing sparsity by reweighted L1 minimization. *Journal of Fourier analysis and applications*, 2008.
- [6] Pasquale Cascarano, Giorgia Franchini, Erich Kobler, Federica Porta, and Andrea Sebastiani. Constrained and unconstrained deep image prior optimization models with automatic regularization. *Computational Optimization and Applications*, 84(1):125–149, 2023.
- [7] Pasquale Cascarano, Elena Loli Piccolomini, Elena Morotti, and Andrea Sebastiani. Plug-and-play gradient-based denoisers applied to ct image enhancement. *Applied Mathematics and Computation*, 422:126967, 2022.
- [8] Antonin Chambolle and Thomas Pock. A first-order primal-dual algorithm for convex problems with applications to imaging. *Journal of mathematical imaging and vision*, 40:120–145, 2011.
- [9] Buxin Chen and et al. Non-convex primal-dual algorithm for image reconstruction in spectral CT. *Computerized Medical Imaging and Graphics*, 2021.

- [10] Qiang Chen, Philippe Montesinos, Quan Sen Sun, Peng Ann Heng, et al. Adaptive total variation denoising based on difference curvature. *Image and vision computing*, 28(3):298–306, 2010.
- [11] Salvatore Cuomo, Mariapia De Rosa, Stefano Izzo, Francesco Piccialli, and Monica Pragliola. Speckle noise removal via learned variational models. *Applied Numerical Mathematics*, 2023.
- [12] Ingrid Daubechies, Ronald DeVore, Massimo Fornasier, and C Sinan Güntürk. Iteratively reweighted least squares minimization for sparse recovery. *Communications on Pure and Applied Mathematics: A Journal Issued by the Courant Institute of Mathematical Sciences*, 63(1):1–38, 2010.
- [13] James F Epperson. *An introduction to numerical methods and analysis*. John Wiley & Sons, 2021.
- [14] Davide Evangelista, Elena Morotti, Elena Loli Piccolomini, and James Nagy. Ambiguity in solving imaging inverse problems with deep-learning-based operators. *Journal of Imaging*, 9(7), 2023.
- [15] Davide Evangelista, James Nagy, Elena Morotti, and Elena Loli Piccolomini. To be or not to be stable, that is the question: understanding neural networks for inverse problems. *arXiv preprint arXiv:2211.13692*, 2022.
- [16] Louise Friot, Françoise Peyrin, Voichita Maxim, et al. Iterative tomographic reconstruction with tv prior for low-dose cbct dental imaging. *Physics in Medicine & Biology*, 67(20):205010, 2022.
- [17] Markus Grasmair. Locally adaptive total variation regularization. In *International Conference on Scale Space and Variational Methods in Computer Vision*, pages 331–342. Springer, 2009.
- [18] Michael Hintermüller and Carlos N Rautenberg. Optimal Selection of the Regularization Function in a Weighted Total Variation Model. Part I: Modelling and theory. *Journal of Mathematical Imaging and Vision*, 59:498–514, 2017.
- [19] Michael Hintermüller, Carlos N Rautenberg, Tao Wu, and Andreas Langer. Optimal Selection of the Regularization Function in a Weighted Total Variation Model. Part II: Algorithm, Its Analysis and Numerical Tests. *Journal of Mathematical Imaging and Vision*, 59:515–533, 2017.
- [20] Jakob S Jørgensen, Christian Kruschel, and Dirk A Lorenz. Testable uniqueness conditions for empirical assessment of undersampling levels in total variation-regularized x-ray ct. *Inverse Problems in Science and Engineering*, 23(8):1283–1305, 2015.
- [21] Avinash C Kak and Malcolm Slaney. *Principles of computerized tomographic imaging*. SIAM, 2001.
- [22] Zhengyang Lu and Ying Chen. Single image super-resolution based on a modified u-net with mixed gradient loss. *signal, image and video processing*, pages 1–9, 2022.
- [23] C McCollough. Tu-fg-207a-04: Overview of the low dose ct grand challenge. *Medical physics*, 43(6Part35):3759–3760, 2016.
- [24] Elena Morotti, Davide Evangelista, and Elena Loli Piccolomini. A green prospective for learned post-processing in sparse-view tomographic reconstruction. *Journal of Imaging*, 7(8):139, 2021.
- [25] Elena Loli Piccolomini and Elena Morotti. A model-based optimization framework for iterative digital breast tomosynthesis image reconstruction. *Journal of Imaging*, 7(2), 2021.
- [26] Monica Pragliola, Luca Calatroni, Alessandro Lanza, and Fiorella Sgallari. On and beyond total variation regularization in imaging: the role of space variance. *SIAM Review*, 65(3):601–685, 2023.
- [27] Leonid I Rudin, Stanley Osher, and Emad Fatemi. Nonlinear total variation based noise removal algorithms. *Physica D: nonlinear phenomena*, 60(1-4):259–268, 1992.
- [28] Emil Y. Sidky and et al. Constrained TpV minimization for enhanced exploitation of gradient sparsity: Application to CT image reconstruction. *IEEE Journal of Translational Engineering in Health and Medicine*, 2014.
- [29] Wim van Aarle, Willem Jan Palenstijn, Jeroen Cant, Eline Janssens, Folkert Bleichrodt, Andrei Dabrovolski, Jan De Beenhouwer, K. Joost Batenburg, and Jan Sijbers. Fast and flexible x-ray tomography using the astra toolbox. *Opt. Express*, 24(22):25129–25147, Oct 2016.
- [30] Wim van Aarle, Willem Jan Palenstijn, Jan De Beenhouwer, Thomas Altantzis, Sara Bals, K. Joost Batenburg, and Jan Sijbers. The ASTRA Toolbox: A platform for advanced algorithm development in electron tomography. *Ultramicroscopy*, 157:35–47, 2015.
- [31] Zhou Wang, Alan C Bovik, Hamid R Sheikh, and Eero P Simoncelli. Image quality assessment: from error visibility to structural similarity. *IEEE transactions on image processing*, 13(4):600–612, 2004.